Real-time Quantification of Polyethylene Crystallinity via In-situ Mid- and Near-infrared Correlation Spectroscopy: Melting and Dissolution

Nicholas Stavinski[a], Ali Ghasemi[b], Luis J. Bruno[a,†], Carmen L. Sánchez Delgado[a,‡], Marina Tsianou[b], Paschalis Alexandridis[b], and Luis Velarde*[a]

[a] Department of Chemistry, University at Buffalo, State University of New York (SUNY), Buffalo, New York, USA

[b] Department of Chemical and Biological Engineering, University at Buffalo, State University of New York (SUNY), Buffalo, New York, USA

Present Address: † University of Puerto Rico at Mayagüez, Puerto Rico 00680; ‡ University of Puerto Rico at Cayey, Puerto Rico 00736

Correspondence: lvelarde@buffalo.edu

Keywords: dissolution, crystallinity, infrared, two-dimensional spectroscopy, polyethylene, polyolefin, chemical recycling

ABSTRACT

Elucidating the crystalline-amorphous interface during decrystallization processes in semi-crystalline polyethylene (PE) is crucial for the advancement of polymer theory and plastic-to-plastic recycling technologies. In this study, we carried out an in-depth investigation of PE thin films undergoing melting or dissolution using a temperature-controlled liquid flow-cell experimental setup which provided in-situ mid-infrared (MIR, 4000-700 cm^{-1}) and near-infrared (NIR, 6000-4000 cm^{-1}) spectra in real time. The spectroscopic results yielded molecular-level information regarding PE decrystallization and chain disentanglement via fundamental vibrations, combination bands, and overtones which were correlated using hetero-spectral two-dimensional correlation spectroscopy (2D-COS). A quantitative procedure for the calculation of PE degree of crystallinity was developed to track transformations of crystalline domains during melting and dissolution. This semi-empirical model achieved a strong linear correlation of at least +0.93 in four spectral regions: 750-700 cm^{-1}, 1500-1400 cm^{-1}, 3000-2800 cm^{-1}, and 4400-4200 cm^{-1}. This analysis revealed important spectral trends about the interfacial solvation environment during these processes. Lastly, the time-evolution of the unraveling, terminal methyl (–CH_3) groups of PE cilia was examined in relation to the decrystallization mechanism of PE. The insights obtained from this study advance the fundamental understanding necessary for developing new depolymerization and recycling strategies.

1 Introduction

Of the 390 million metric tons (Mt) of plastics produced across 44 countries, roughly 174 Mt are packaging materials (e.g., thin plastic films), most of which are polyolefins such as high-, low-, and linear low-density polyethylene (HDPE, LDPE, and LLDPE, respectively) and polypropylene [1,2]. Thin film plastics are challenging to recycle at materials recovery facilities due to their flexibility, low density, and multi-component layers, yet research has shown there are economic incentives for these materials if the recycled product yield and product price is improved [3]. Closing the recycling loop of packaging films may be achievable with new measurement techniques [4-8] and solvent-based separation methods [9-13]. Regarding the latter, recent modeling and parametric analyses of cellulose [14-16], polyester [17], and polystyrene [18] dissolution may prove to be one such pathway for future "plastic-to-plastic" conversion technologies.

The unit cell of PE possesses an orthorhombic configuration at ambient conditions which gives rise to factor group splitting [19,20]. Due to the lateral crystal vibrations of PE's methylene (–CH_2–) modes, doublet IR-active bands corresponding to in- and out-of-phase signals for "rocking" (ρ), "scissoring" (δ), symmetric stretching (ν_s) and anti-symmetric stretching (ν_{as}) motions appear at energies of 750-700 cm^{-1}, 1500-1400 cm^{-1}, and 3000-2800 cm^{-1}, respectively. Structural investigations of PE have been reported using X-ray diffraction [21-24], wide-angle X-ray scattering [20,25,26], mechanical deformation tests [27], differential scanning calorimetry (DSC) [28,29], Raman spectroscopy [30-35], infrared spectroscopy [36-39], nuclear magnetic resonance spectroscopy [40,41], and molecular dynamics simulations [42-46]. At present, however, there are no direct solid-state measurements detailing a molecular-level mechanism of decrystallization for recalcitrant semicrystalline PE under realistic dissolution conditions where small solvent molecules diffuse into the polymeric matrix and induce the disentanglement of rigid, well-ordered, chains. Key fundamental questions revolve around the emerging solvation structures and mechanistic stages of disentanglement of solid PE chains in contact with a surrounding solvent.

Here, dynamic mid-IR (MIR, 4000-400 cm^{-1}) and near-IR (NIR, 14286-4000 cm^{-1}) vibrational spectra of PE are acquired simultaneously using an FT-IR spectrometer that is capable of scanning from 8000 to 350 cm^{-1} —a region that contains PE's fundamental vibrational modes, combination bands, and overtones. Using two-dimensional correlation spectroscopy (2D-COS), an analytical technique developed by Noda and co-workers [47-52], alterations in PE chain structures in the MIR and NIR regions were examined under melt and dissolution conditions. 2D-COS has positively-impacted research fields including, but not limited to, protein dynamics [53-58], coordination chemistry [59,60], nanomaterials [61-64], biomedicine [65-67], drug mixture analysis [68], and polymers [69-73] through its ability to provide structural insights of dynamic molecular systems that would otherwise be indiscernible based on one-dimensional (1D) spectra alone. This is accomplished via a cross correlation analysis of two spectral variables (e.g., IR frequency, Raman shift, wavelength) that undergo changes from an external perturbation (e.g., time, temperature).

Real-time *in situ* MIR and NIR spectra of PE undergoing dissolution are reported for the first time in this work. Temporal variations of key vibrational peak intensities and frequency shifts due to van der Waals interactions and polymer solvation revealed intrinsic differences in the decrystallization mechanism of PE under melting and dissolution conditions. The correlation of IR bands originating from chain conformations and various vibrational modes such as, "rocking" CH_2 groups, combination bands, and end chain CH_3 groups, may advance parametric analyses of dissolution-precipitation models, assist with the fabrication of PE-based membrane materials, and advance fundamental PE "crystallization theory" —a topic that remains an outstanding challenge in macromolecular polymer science [74]. Furthermore, after confirming and adjusting MIR and NIR mode assignments that are traditionally reported in tabular format, new IR-active vibrational modes were identified and tentatively assigned via 2D-COS. Leveraging these findings, a quantitative spectroscopic model was constructed to provide real-time *in situ* crystallinity insights for PE or PE-containing materials undergoing crystalline-to-amorphous transformations.

2 Materials and Methods

2.1 Materials

HDPE (0.952 g/cm^3, melt index=2.0 g/10 min., melt point=128 °C, P/N:GE7252) was graciously provided by Braskem U.S.A (Figure 1A); *p*-xylene (≥99+ %, P/N:296333-1L) was purchased from Sigma-Aldrich (Figure 1B); LDPE (0.925 g/cm^3, melt index=25 g/10 min., melt point=116 °C, P/N:420843) and LLDPE (0.918 g/cm^3, melt index=1 g/10 min., melt point=120.9 °C, P/N:428078) were purchased from Sigma-Aldrich. PE thin films were prepared by placing approximately 25 PE pellets inside a custom brass ring mold (260 brass shim stock P/N:9011K201 McMaster-Carr®, 85 millimeter (mm) outer diameter, 60 mm inner diameter, and 0.05 mm thickness which was wrapped inside film made from Teflon® PTFE (McMaster-Carr®, P/N:8569K36). Then, the sample mold was transferred to a pre-heated hydraulic press (Carver®, Inc., 180 °C). For 5 minutes, 4000 pounds of force was applied to generate HDPE films of uniform thickness; thermal expansion[75] was observed and compensated for via modification of mold thickness, providing the desired film thicknesses of 0.05 mm and 0.1 mm. Electronic calipers (McMaster-Carr®, increment=0.01 mm, P/N:4996A51) confirmed the thickness of the polymer films. Individual samples were cut using a scalpel from the bulk mold to achieve the desired dimensions of 5×5×0.05 mm.

2.2 Differential Scanning Calorimetry

Melting point and enthalpy of fusion of the PE samples were determined via DSC using a TA Instruments Q200 (Supporting Information). Pellets and films were prepared and crimped into Tzero aluminum pans (TA Instruments, P/N:901683.901) and lids (TA Instruments, P/N:901671.901). An argon flow rate of 50 mL/min. was used for each measurement. Samples were equilibrated at 0 °C before being heated to 200 °C at a rate of 5 °C/min. Then, samples were cooled at 5 °C/min. to 0 °C. Degree of crystallinity of the pellets was calculated using the second cycle (Table S1). In this study, enthalpy of fusion is taken to be 293 J/g according to Wunderlich and Czornyj [76]; since then, similar values have also been reported[25]. Experimental uncertainty of DSC results is ±1%. For validation of the quantitative FT-IR method, average crystallinity of HDPE thin films (5×5×0.05 mm) was determined to be 65 % using the second cycle.

2.3 In-situ Temperature-controlled FT-IR Setup

A temperature-controlled demountable liquid flow cell (Harrick Scientific TFC-S25) connected to a temperature controller (Harrick Scientific ATC-024-3, 50/60 Hz, 115VAC, 3.0 AMP) was used for the FT-IR experiments. Sample heating was PID-controlled for linear ramping to the desired temperature by the controller and cooling occurred slowly under ambient conditions (22 ± 1 °C).

A three-dimensional rendering of the FT-IR liquid cell is shown in Figure 1C (Autodesk Fusion 360). Film dimensions of 5×5×0.05 mm were determined using electronic calipers. Zinc selenide (ZnSe, Crystran Ltd., 25×2 mm polished) was selected for its MIR and NIR transmission and independence from temperature-induced spectral effects.[77] Adhesion of the PE films to the ZnSe was accomplished inside a ventilation hood by placing the substrate onto a hotplate (130 °C) for 4 minutes or until the film became transparent. Care was taken to ensure the films were not degraded. The melt was then slow-cooled to room temperature.

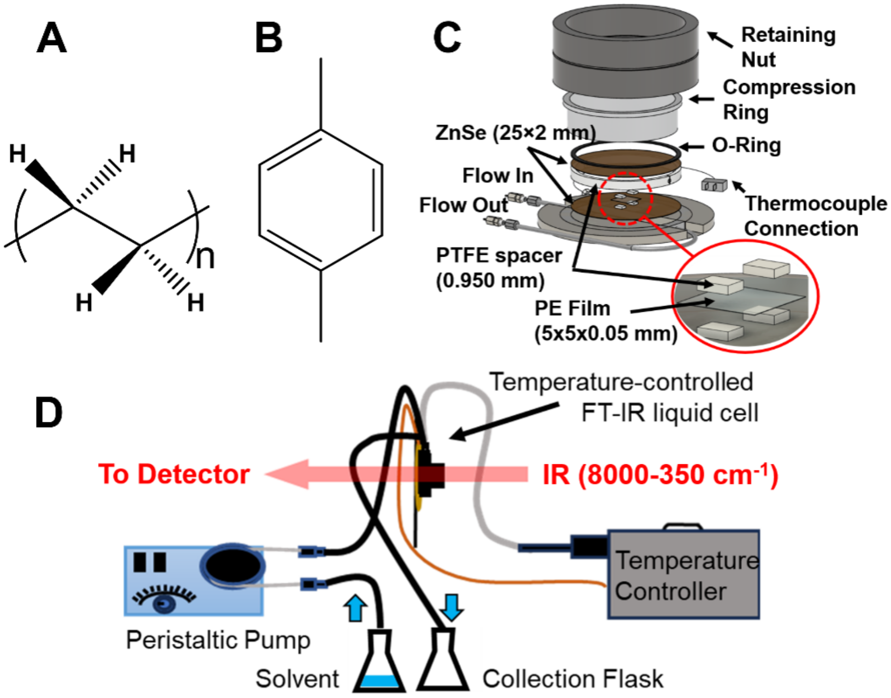

FIGURE 1. (A) Polyethylene monomeric unit and (B) *p*-xylene molecular structure. (C) Schematic of heated liquid cell and positioning of the polymer sample. (D) Layout of the temperature-controlled FT-IR spectroscopy experimental setup.

To prepare the liquid flow cell, a 0.950 mm thick PTFE spacer (Harrick Scientific) was placed between the two ZnSe optical windows (Figure 1C). Next, two Viton O-rings were placed beneath and atop the windows. Then, a compression ring and retaining nut were threaded together. Stainless-steel Swagelok tube fittings (union, 1/8” tube OD) and stainless-steel hose connectors (1/8” tube adapter, 1/8” hose ID) were used to join the flow cell with chemically-inert, high-temperature Viton fluoroelastomer tubing (McMaster-Carr, 1/8” ID, 1/4" OD). Two 150 mL Erlenmeyer flasks were connected to the Viton tubing, one flask containing fresh solvent and the other serving as a waste collection flask. Parafilm wrap (Bemis Co.) was used to seal the solvent system at the opening of each flask. A variable flow peristaltic pump (Fisherbrand, 0.4-85 mL/min., 120 V 60Hz, 115VAC power supply) transported solvent to the FT-IR cell in 15-30 seconds using a rate equivalent to ~80% of the maximum flow setting. The peristaltic pump was turned off once the liquid cell was filled and FT-IR measurements were performed immediately after the pump shut-off (Figure 1D).

2.4 FT-IR Spectroscopy

A Bruker VERTEX 70 FT-IR spectrometer (Billerica, MA, USA) equipped with a liquid-nitrogen-cooled mercury cadmium telluride detector (LN2-MCT) was used to acquire transmission MIR (air-cooled ceramic source) and NIR (air-cooled tungsten source) spectra (1 mm aperture, 1 sample scan, 64 background scans, 2 cm^{-1} resolution, zero-second delay between repeated measurements). The detector setup achieves a spectral coverage of 8,000-350 cm^{-1} per MIR/NIR spectrum acquisition. However, an optimal scan range of 6000-500 cm^{-1} and per spectrum acquisition time of 3.475 seconds were used in this study. Measurements were carried out at a scan velocity of 10 kHz using double-sided forward-backward acquisition mode at a resolution of 2 cm^{-1}. Faster acquisitions could be achieved with a lower resolution and/or higher mirror velocity at a cost of signal-to-noise ratio (SNR), but our melting and dissolution study did not warrant the need for faster acquisition rates (further details in Supporting Information Section 3). Attenuated-total reflectance Fourier-Transform infrared spectroscopy (ATR-FTIR), equipped with a single-reflection (45° angle) ZnSe unit (PIKE Technologies, Madison, WI, USA), was used for its surface-sensitivity to compare with transmission FT-IR. Depth of penetration of the ATR-FTIR evanescent wave was calculated by supplying Equation S1 with optical constants

(Supporting Information). Time increments between spectral acquisitions were validated using a stopwatch. The OPUS 7.5 software package was used to collect and process the data. The Python programming language (3.12.0 courtesy of the Python Software Foundation) was used inside a Jupyter notebook (6.3.0 courtesy of Project Jupyter) to visualize spectra.

TABLE 1. Comprehensive summary of reported infrared vibrational bands of PE.

IR Frequency (cm^{-1})	**Wavelength (µm)**	**Wavelength (nm)**	**Phase**	**Vibration**	**Intensity**	**Ref.**
200	50.0	50,000	---	---	VW	[78]
543	18.4	18,416	---	---	W	[78]
600	16.7	16,666	---	---	VW	[78]
713-716	14.0	14,005	Non-crystalline, monoclinic-like *trans*	$\rho(CH_2)$	VW	[79,80]
719-721	13.9	13,888	Orth.	$\rho(CH_2)$ (out-of-phase “rocking”)	M	[19,78,79, 81]
718-720	13.9	13,869	Amorph.	---	W	[81]
729-730	13.7	13,717	Orth.	$\rho(CH_2)$ (in-phase “rocking”)	M	[19,78,79, 81]
888	11.3	11,261	---	$\rho(CH_3)$	VW	[78]
965	10.4	10,363	---	---	VVW	[78]
1065	9.39	9,389	---	ν(CC)	VW	[78]
1080	9.26	9,259	Amorph.	ν(CC)	VW	[78]
1110	9.01	9,009	---	---	VVW	[78]
1150	8.69	8,696	---	---	VVW	[78]
1170	8.55	8,547	---	---	VVW	[78]
1306	7.65	7,657	Conf. (*gtg'*)	$\omega(CH_2)$ (“wagging”)	W	[70,78,82]
1339	7.47	7,468	Conf. (*eg*)	$\omega(CH_2)$ (“wagging”)	VW	[70,78]
1352	7.39	7,396	Conf. (*gg*)	$\omega(CH_2)$ (“wagging”)	W	[70,78]
1365	7.33	7,326	Conf. (*gtg*)	$\omega(CH_2)$ (“wagging”)	W	[70,78]
1377	7.26	7,262	Orth.	$\delta(CH_3)$ (“umbrella” branching)	W	[78,82]

1450-1455	6.90	6,896	Amorph.	short *trans* sequences	---	[79]
1463	6.84	6,835	Orth.	$\delta(\mathrm{CH}_2)$ (out-of-phase “scissoring”)	S	[19,78,81]
1466-1467	6.84	6,835	Amorph.	long *trans* disordered sequences	M	[81]
1470	6.80	6,803	Orth.	$\delta(\mathrm{CH}_2)$ (in-phase “scissoring”)	S	[19,78,81]
1473-1475	6.79	6,789	Non-crystalline, monoclinic-like *trans*	---	VW	[83]
1710	5.85	5,848	---	---	VW	[78]
1805	5.54	5,540	---	---	VVW	[78]
1890	5.29	5,291	---	---	VW	[78]
2010	4.98	4,975	---	---	VW	[78]
2130	4.69	4,695	---	---	VVW	[78]
2295	4.36	4,357	---	---	VW	[78]
2640	3.79	3,788	---	---	W	[78]
2848-2850	3.51	3,506	Orth.	$\nu_s(\mathrm{CH}_2)$ symmetric	VS	[19,78,82]
2851-2852	3.51	3,506	Amorph.	---	---	---
2872-2899	3.48	3,482	Orth.	$\nu_s(\mathrm{CH}_3)$ symmetric	W	[78]
2915-2920	3.42	3,425	Orth.	$\nu_{as}(\mathrm{CH}_2)$ anti-symmetric	VS	[19,78,82]
2921-2922	3.42	3,424	Amorph.	---	---	---
2960	3.38	3,378	Orth.	$\nu_{as}(\mathrm{CH}_3)$ anti-symmetric	VW	[78]
4022	2.49	2,486	Orth. (⊥)	---	---	[84]
4094	2.44	2,443	Orth. (⊥)	---	---	[84]
4198	2.38	2,382	Orth. (⊥)	---	---	[84]
4221	2.37	2,369	Orth. (‖)	$\nu_{as}(\mathrm{CH}_2) + \omega(\mathrm{CH}_2)$	---	[84]
4250-4252	2.35	2,351	Orth. (⊥)	$\nu_s(\mathrm{CH}_2) + \delta(\mathrm{CH}_2)$	---	[82,84]
4256	2.35	2,349	Hex. (⊥)	$\nu_s(\mathrm{CH}_2) + \delta(\mathrm{CH}_2)$	---	[37]
4259-4261	2.35	2,348	Amorph.	---	---	[84]
4265-4269	2.34	2,345	Conf. sequences (*gtg*, *gg*, *gtg′*)	---	---	[69]
4290	2.33	2,331	Orth.	---	---	[69]

4320-4323	2.31	2,313	Orth. (⊥)	$\nu_{as}(CH_2) + \delta(CH_2)$	---	[69,82,84]
4330-4332	2.31	2,308	Amorph.	---	---	[84]
4342	2.30	2,303	Orth. (⊥)	$\nu_{as}(CH_2) + \delta(CH_2)$	W	[69,84]
4349	2.29	2,299	Hex. (⊥)	$\nu_{as}(CH_2) + \delta(CH_2)$	---	[84]
5640	1.77	1,773	Amorph.	---	---	[69]
5663-5665	1.77	1,765	Orth. (⊥)	$2\nu_s(CH_2)$, first overtone	W	[84,85]
5671-5675	1.76	1,763	Amorph.	$2\nu_s$	VW	[82]
5710-5720	1.75	1,751-1,748	Amorph.	Terminal symmetric CH_3 + CH_2 *gauche*, first overtone	VW	[38]
5732-5734	1.75	1,745	Orth. (⊥)	---	VW	[84]
5774-5778	1.73	1,731	Orth. (⊥)	$2\nu_{as}(CH_2)$, first overtone	W	[82,84,85]
5784-5788	1.73	1730-1727	Amorph.	$2\nu_{as}$	VW	---
5810	1.72	1,721	Amorph.	---	VVW	[84]
5840-5848	1.71	1,710	Amorph.	Terminal CH_3, first overtone	VW	[38,69,85]
5914-5917	1.69	1,690	Amorph.	Short branch CH_3, first overtone	VVW	[38]

Notes:

a Amorph.: amorphous; Orth.: orthorhombic; Hex.: hexagonal; Conf.: conformational defect

b g="gauche"; t="trans"; eg="end gauche"

c VW: very weak; W: weak; M: medium; S: strong; VS: very strong

d (||), vibrational direction aligned parallel to incident light; (⊥) vibrational direction aligned perpendicular to incident light; for NIR study on polarized PE samples see Watanabe et al. [84]

2.5 Generalized 2D-COS Procedure

The theory of infrared 2D-COS was pioneered by Noda [47,49] (see Supporting Information). In brief, 1D spectra are spread across two dimensions via a mathematical procedure called a cross-correlation analysis. The real and imaginary components of the complex cross-correlation function are calculated along a variable (e.g., time) for two signals (e.g., IR spectra) that undergo a perturbation (e.g., melting, dissolution). Two resultant variations in signals are acquired from the mathematical formalism, namely synchronous and asynchronous 2D spectra. The synchronous 2D spectrum represents simultaneous spectral changes of the dynamic 1D spectra and it reflects alterations in IR band area over the perturbation variable. The asynchronous 2D spectrum is unique because it represents out-of-phase changes in the dynamic 1D spectra and it may achieve enhanced spectral resolution and deconvolute overlapped IR bands that would be otherwise hidden in a set of 1D spectra. For example, asynchronous spectra may provide evidence for IR-active vibrations that are changing at different rates across the perturbation variable. Thus, with informed chemical knowledge, these changes may be used to elucidate congested spectral regions that contain vibrations of different molecular origin.

The 2D-COS analysis was caried out using the 2Dpy package developed by Morita and co-workers [71,86-89]. Red-colored bands represent a positive correlation intensity, and blue-colored bands represent a negative correlation intensity; both of which are with respect to the perturbation variable.

2.6 Quantification of Degree of Crystallinity

Using a Lorentzian lineshape, integrated areas of the crystalline, I_{crystal}, and amorphous, $I_{\mathrm{amorphous}}$, bands were acquired using the IGOR Pro 9 multi-band fitting package. Degree of crystallinity, x_{c}, is defined as

$$x_{\mathrm{c}} = \frac{I_{\mathrm{crystalline}}}{I_{\mathrm{crystalline}} + (\alpha I_{\mathrm{amorphous}})} * 100\ \% \qquad (1)$$

where the coefficient α represents a value that accounts for intrinsic IR band intensity variations between the crystalline and amorphous bands. For the $\rho(CH_2)$ bands between 750-

700 cm^{-1}, α is equal to 1.2.[81] For all other semi-crystalline regions reported in this study, α is defined as

$$\alpha = \frac{I_{\mathrm{crystalline,intrinsic}}}{I_{\mathrm{amorphous,intrinsic}}} \qquad (2)$$

where the integrated areas of the intrinsic crystalline, $I_{\mathrm{crystal.,intr.}}$, and intrinsic amorphous, $I_{\mathrm{amorph.,intr.}}$, bands were determined by band-fitting of the initial crystalline component and final amorphous component of each experimental trial, respectively. The subsequent IR band parameters were fixed for the determination of x_{c} as a function of time with only the band integration area set as a variable (see Supporting Information for standard deviation).

2.7 Data Analysis

Principal component analysis (PCA) was performed inside a Jupyter notebook (6.3.0, Python 3.12.0). 250 FT-IR spectra representing dissolution and melting time evolution from initial x_{c} to 0 % (13 minutes elapsed) were assessed using the principal axis method to validate the 2D-COS results. Specifically, this method extracts the maximum variance from each variable that was identified via a search of all linear combinations, reducing the dimensionality of the data to provide orthogonal factors. The spectral region from 735-705 cm^{-1} was evaluated to minimize training and testing of spectral artifacts that appeared outside of this range. PCA space for principal component 1 (PC1) and principal component 2 (PC2) was visualized using shaded-color regions for each class label. A correlation matrix was generated inside a Jupyter notebook (6.3.0, Python 3.12.0) using the Pandas, Matplotlib, and Numpy packages. Imbalanced datasets containing degree of crystallinity values were truncated and appended to zero (i.e., 0 % crystallinity) to generate average x_{c} over time.

3 RESULTS AND DISCUSSION

3.1 2D-COS of HDPE Melting: Chain Conformations and Crystal Defects

Flory *et al*. **[90]** coined the term “interphase” to describe the transition layer between the crystalline lamellae and amorphous regions [44]. Now it is commonly agreed upon [40,44] that the semi-crystalline PE structure consists of four components: (1) an orthorhombic crystal phase with the chains in an all-*trans* conformation, (2) a non-crystalline amorphous phase with chains in *gauche* conformations which are susceptible to rapid re-orientation, (3) an interphase where chains demonstrate an all-*trans* conformation and have increased mobility compared to the rigid orthorhombic all-*trans* conformation, and (4) an interphase with equilibrium *gauche* conformations that have reduced mobility compared to the gauche conformers comprising the highly-mobile amorphous phase. Under high temperatures and pressures, other PE crystalline phases may exist such as the hexagonal [22,24,26,37,41,84,91-93] and monoclinic [22,26,79,91,94,95] unit cell configurations. Various characterization techniques such as X-ray diffraction/scattering and DSC have been used to study the crystalline-to-amorphous phase transition in PE; however, these techniques can pose challenges for receiving real-time in-situ measurements of a polymeric system undergoing perturbation (e.g., polymer dissolution). Here, we demonstrate the use of in-situ ATR-FTIR to study the evolution of the interphase of PE under dissolution conditions. To do this, we first examine PE’s vibrational modes and subsequent structural changes under melt conditions (Figure 2).

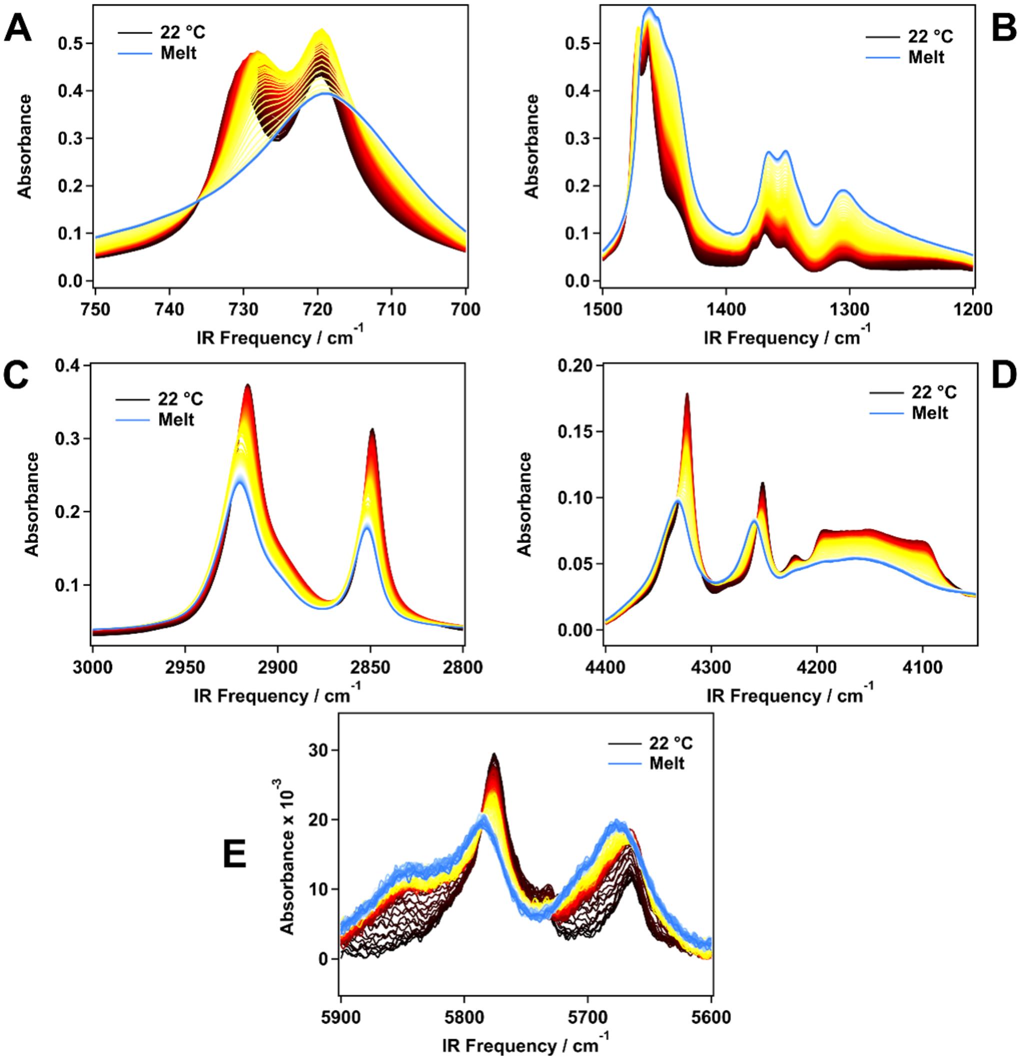

FIGURE 2. Transmission infrared spectra of HDPE melting from 22 °C (black) to 135 °C (blue) acquired via temperature-controlled ATR-FTIR spectroscopy in the following spectral ranges: (A) 750-700 cm^{-1} , (B) 1500-1200 cm^{-1} , (C) 3000-2800 cm^{-1} , (D) 4400-4050 cm^{-1} , and (E) 5900-5600 cm^{-1}.

The out-of-phase and in-phase, $\rho(CH_2)$, modes, reporting on the lateral vibrational interactions within PE's orthorhombic unit cell, appear at 719 cm^{-1} and 729 cm^{-1}, respectively (Figure S28A). A broad band at 718 cm^{-1} corresponding to the amorphous phase is revealed after the crystalline domains become disordered during melting (Figure 2A). The amorphous band was consistently observed in multiple trials in which heating rate, resin manufacturer, and sample thickness were varied; this band corresponds to PE chains that have no preferential orientation or chain ordering, and this is reflective of a PE sample that is in a disordered state or molten form. This band's susceptibility to frequency shifting in the presence of solvent molecules is addressed in Section 3.2.

Figure 3 provides the 2D-COS results for HDPE melting observed in two regions-of-interest: (1) the "rocking" $\rho(CH_2)$ region at 750-700 cm^{-1} and (2) the combination bands at 4400-4200 cm^{-1}. In Figure 3A, along the diagonal (where both spectral variables, ν_1 and ν_2, converge), two auto-bands of positive correlation intensity (red color) appear. Auto-bands in synchronous 2D-COS spectra signify spectral intensity variations that are products of the auto-correlation function observed over time, *t*; they appear along the diagonal axis. Regions with greatest intensity changes over *t*, with regards to the reference spectrum, $\bar{A}(\nu j)$, generate the darkest-colored auto-bands. In Figure 3A, the strongest intensity appears at the 729 cm^{-1} auto-band, which represents the decrease in absorbance of the $\rho(CH_2)$ band. A positive off-diagonal correlation exists between the "in-phase" $\rho(CH_2)$ mode at 729 cm^{-1} and the "out-of-phase" $\rho(CH_2)$ mode at 719 cm^{-1}; this observation is confirmed by the second auto-band along the diagonal axis, where the reduced intensity (i.e., a lighter red color) is indicating the appearance of the amorphous band at 720 cm^{-1} after 6.5 minutes. Cross-bands are located off the diagonal, and they are representative of simultaneous changes of ν_1 and ν_2. For the synchronous spectrum in Figure 3B, cross-bands appear at 712 cm^{-1} and 719 cm^{-1}. These bands reflect simultaneous intensity alterations from the perturbation variable, *t*, and they correspond to a coupled-to or similarity in vibrational signatures depending on their positive or negative phasing.

Asynchronous spectra represent out-of-phase behavior (i.e., dissimilarity or unsynchronized spectral changes) with respect to the system. They showcase spectral changes arising from vibrational signatures of different physical origins. There are no auto-bands in asynchronous spectra; they contain only cross-bands, which appear from two dynamic spectral intensities that occur delayed or accelerated with respect to the reference state. Characterized by a "splitting" along the diagonal axis, bands of either correlation intensity, positive (red) or negative (blue), may suggest the presence of a new spectral feature (i.e., an IR-active vibrational mode that is unobservable in dynamic 1D spectra). Asynchronous spectra have utility in de-convoluting congested spectra, revealing bands of different molecular origins. In Figure 3C, four bands are observed in the asynchronous spectrum of PE melting: (1) 712 cm^{-1}, (2) 719 cm^{-1}, (3) 729 cm^{-1}, and (4) 731 cm^{-1}. The bands at 719 cm^{-1} and 729 cm^{-1} corresponding to the $\rho(CH_2)$ out-of-phase and in-phase "rocking" motions, respectively, have been already discussed here. The bands at 712 cm^{-1} and 731 cm^{-1} are inapparent through one-dimensional FT-IR and have not been previously observed in HDPE melting and dissolution. Therefore, their role in the context of fundamental PE crystallization theory and quantitative modeling needs to be understood.

Considering a report of the 1D spectra of LDPE nanocomposites [79], it is reasonable to deduce that the 712 cm^{-1} band in this study may correspond to the so-called "monoclinic-like" structure. At ambient conditions, the orthorhombic crystal configuration is thermodynamically-favored; however, deformation of the crystalline domains influenced by stress, or a force, can shift the favorability to a monoclinic configuration [46,96,97]. It is important to note that the presence of monoclinic-like IR bands does not necessarily mean that well-ordered monoclinic crystals are present in the PE film. In fact, according to Bernazzani and coworkers [98], the monoclinic-like and amorphous components are together classified as non-crystalline phases. The presence of monoclinic structure is often taken for granted in literature [79,83]. Further confirmation of the presence of the monoclinic-like arrangement in this study's samples is shown in Figure S18 by the band at 1473 cm^{-1} corresponding to all-trans CH_2 bending. While the commonly reported 729 cm^{-1} band corresponds to a well-formed orthorhombic crystal, the higher frequency and overlapping 731 cm^{-1} band may arise due to a crystal structure that is more disordered or contains defects. This previously unreported band at 731 cm^{-1} is tentatively attributed to a gauche crystal defect.

Hetero-spectral 2D-COS results detailing correlations between the 750-700 cm^{-1} and 4350-4200 cm^{-1} spectral regions are reported in Figure 3B and 3D. In Figure 3D, a negative correlation is observed for the $\nu_s(CH_2) + \delta(CH_2)$ combination band at 4252 cm^{-1} and $\nu_{as}(CH_2) + \delta(CH_2)$ at 4322 cm^{-1} with respect to the 712 cm^{-1} band. Moreover, in

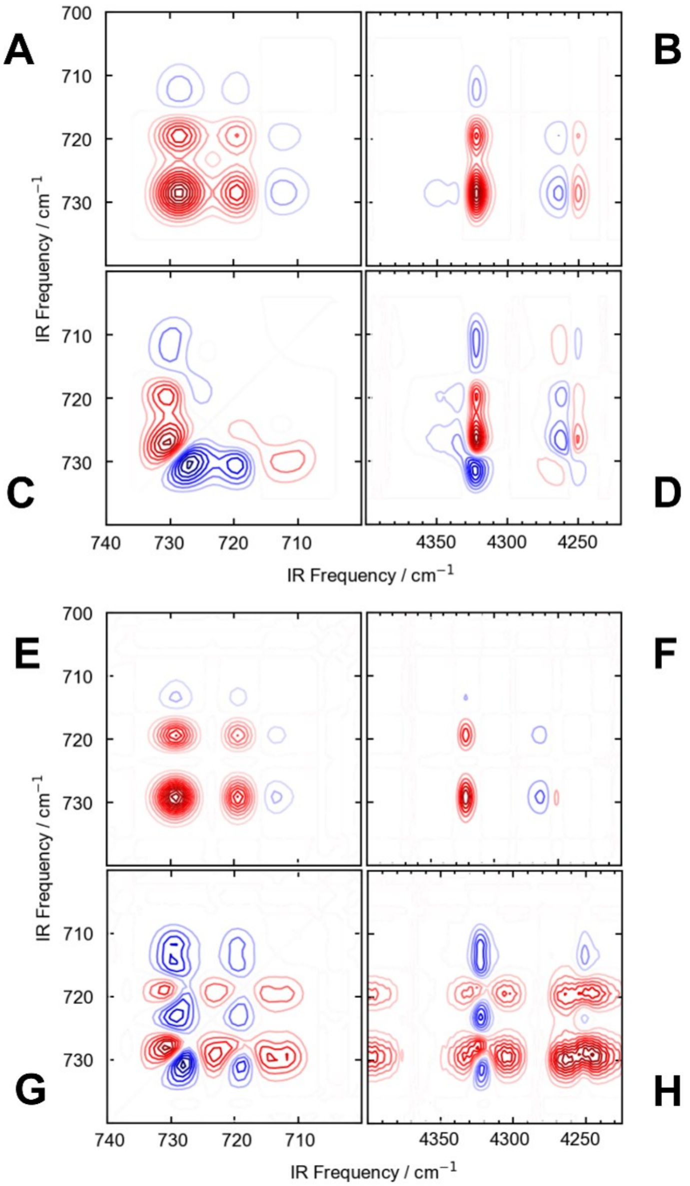

FIGURE 3. HDPE melting from 22 °C to 130 °C. (A) Synchronous spectrum 750-700 cm^{-1}. (C) Asynchronous spectrum 750-700 cm^{-1}. (B) Heterospectral synchronous spectrum 750-700 cm^{-1} and 4350-4200 cm^{-1}. (D) Heterospectral asynchronous spectrum 750-700 cm^{-1} and 4350-4200 cm^{-1}. HDPE dissolution in *p*-xylene at 106 °C. (E) Synchronous spectrum 750-700 cm-1. (F) Heterospectral synchronous spectrum 750-700 cm^{-1} and 4350-4200 cm^{-1}. (G) Asynchronous spectrum 750-700 cm^{-1}. (H) Heterospectral synchronous spectrum 750-700 cm^{-1} and 4350-4200 cm^{-1}. Red and blue patterns indicate bands with positive and negative correlation intensity.

Figure 3D, the presence of the amorphous band at 4260 cm^{-1} with a positive correlation at 712 cm^{-1} implies the non-crystalline origins of the 712 cm^{-1} band. This provides further evidence of the existence of a non-perfect crystalline component within the samples. The 731 cm^{-1} band also displays a positive correlation with respect to the 4260 cm^{-1} amorphous band. This may be due to the PE chains existing under a more-constrained environment within the polymeric matrix and therefore lesser in molecular population relative to the *ρ*(CH_2) modes. Thus, it may be deduced that the band at 731 cm^{-1} corresponding to a crystal defect is buried beneath the out-of-phase "rocking" crystalline band at 729 cm^{-1}. A pedagogical guide explaining the interpretation of asynchronous splitting was provided by Noda [99].

The monoclinic-like conformations are found within the core of PE films rather than on the surface, which was observed to have a predominantly orthorhombic crystalline arrangement via ATR-FTIR (Figure S15). This finding is important for dissolution studies and, more-broadly, polymer-liquid interfacial research, as the presence of small, non-polar solvent molecules may influence the crystalline-to-amorphous phase behavior through thermodynamic and/or kinetic mechanisms that would not be anticipated if based solely on de-crystallization reports for pristine polymers. Since the films used in this study were produced using a heated hydraulic press, control experiments were performed to ensure consistency in the semi-crystalline structure of all samples prior to melt adhesion to the ZnSe optical window. Specifically, DSC confirmed the absence of any well-developed, second crystal fractions (monoclinic or hexagonal), as the endotherm in Figure S2-4 (Supporting Information) revealed a single melting transition at 129.3 °C. Furthermore, the PE pellets were subjected to 0.028 GPa of pressure and 180 °C to generate thin films. The minimum pressure and temperature required for PE to undergo a phase transition and produce monoclinic crystals is 6 GPa (Figure S28). Further investigation of the interfacial ordering of the non-crystalline monoclinic-like trans conformer is necessary for future, real-world applications. Surface morphology studies of semi-crystalline polymers remains an exciting research area [27,100-102].

3.2 2D-COS of HDPE Dissolution: Infrared Frequency Jumps

Figures 3E-3H show 2D-COS results for HDPE dissolution in *p*-xylene as a function of time. Best observed in the asynchronous spectrum in Figure 3G, a new IR band absent in Figure 3C appears at 724 cm^{-1} of opposite correlation phase to that of the two crystal bands at 719 cm^{-1} and 729 cm^{-1}. It can be inferred that this band corresponds to amorphous polymer. While the amorphous band for HDPE melting appears at 718 cm^{-1}, the band at 724 cm^{-1} was observed to shift (or "jump") to higher IR frequency over time (Figure S11) during dissolution. The typical spectral behavior of this amorphous band can be visualized in Figure 4A, where a 2D contour plot shows the band's tendency to narrow in its full-width-at-half-maximum (FWHM) after a 13-minute time interval while maintaining a centered IR band frequency of 718 cm^{-1}. However, for the dissolution experiment (Figure 4B), the amorphous region broadens in its FWHM before achieving a centered frequency of 724 cm^{-1}. This phenomenon was observed for each of the different PE melting and dissolution experiments performed (Figure S11, S12). To the best of our knowledge, the behavior of this amorphous vibrational mode during dissolution has not been reported.

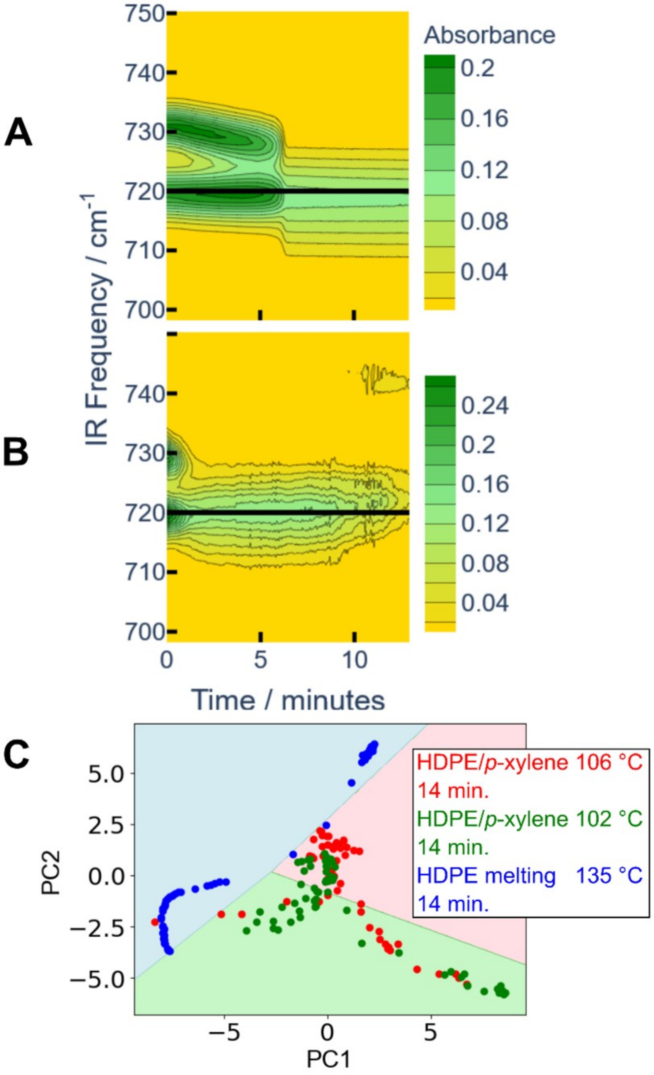

FIGURE 4. Two-dimensional contour plot of (A) HDPE melting and (B) HDPE dissolution at 106 °C in *p*-xylene. The black line at 720 cm^{-1} is for reference. (C) PCA of HDPE lineshape alterations at 735-705 cm^{-1}. HDPE dissolution at 106 °C (red), HDPE dissolution at 102 °C (green), and HDPE melting (blue).

The work of Tiemblo et al. provided 1D spectra of amorphous LDPE with spherical, fibrous, and lamellar nanofillers [79]. In their work, the conformational structure of LDPE with fillers was determined to vary from that of unblended LDPE, which the authors attributed to constraint of the PE chains in a given composite. A similar mechanism for solid-liquid systems may be responsible for the behavior of the 724 cm^{-1} amorphous band. In fact, due to the presence of non-polar solvent molecules, the frequency shift for the *gauche*-conformer amorphous band from 720 cm^{-1} to 724 cm^{-1} may be attributed to the arising electrostatic forces due to PE-solvent interactions. While the *gauche* conformers are present for highly-mobile PE chains which have underwent de-crystallization regardless of solvent presence, it is reasonable to posit that a thermodynamically-preferred *gauche* conformer of an orientation exhibiting increased steric hinderances is responsible for higher-IR frequency CH_2 vibrations.

The IR absorbance of the PE films was greater under dissolution conditions than melting (Figure 4A and Figure 4B). According to the Beer-Lambert Law, a given material's absorbance depends upon the mathematical product of its (1) molar absorptivity, (2) path length (i.e., PE film thickness), and (3) moles per unit volume. The observed increase in absorbance may suggest an increase in the molar absorptivity or in the number density along the path length. For instance, Mrad, McKenna, and co-workers reported increased swelling percentage for less-dense PE samples in the presence of alkanes [103]. However, future reports explaining macro-molecular structural changes (i.e., spherulite transformations in three-dimensions) under dissolution are needed. Regardless, it may be inferred that swelling of the PE chains contributes to the formation of the interphase where there is a large equilibrium *gauche* conformer of reduced reorientation compared to chains in absence of solvent. Specifically, a force applied to the crystalline and non-crystalline domains stretches the chains, re-orienting the configuration of the lateral $\rho(CH_2)$ vibrations. The resultant IR-active vibrational interactions are of increased frequency due to this meta-stable state as the chains eventually dissolve into their monomeric units as reflected by the gradual decrease in absorbance after 5 minutes (Figure 4B).

For alkanes, the phase transition from solid-state *trans* chain conformations to liquid-state *gauche* chain conformations has been well-studied [104-106], with recent reports elucidating interface-specific phenomena with monolayer specificity [107]. Experimental variables such as temperature, solvent, film thickness, and correlation to other vibrations have largely gone under-represented in chemical systems with real-world implications. Sections 3.1 and 3.2 demonstrate the utility of scientific computing techniques applied to spectral data that could potentially be scaled up to inform processing at chemical recycling facilities. Specifically, the melt results are compared side-by-side with dissolution results, providing experimental evidence of solvent effects. Therefore, future work utilizing different spectroscopic probes (e.g., Raman, X-ray) and custom flow cells for in-situ studies will further enhance the field's understanding of PE's order-to-disorder transition during decrystallization as exemplified by this work.

3.3 Orthogonality of $\rho(CH_2)$ Behavior: Melting and Dissolution

To expand upon the results presented in Figures 4A and 4B, PCA was applied as a dimensionality reduction technique to three separate HDPE de-crystallization experiments: HDPE dissolution at 106 °C (Figure 4C, red), HDPE dissolution at 102 °C (Figure 4C, green), and HDPE melting (Figure 4C, blue). PCA reduces the dimensionality of a large set of variables by transforming them into a smaller set of variables that retain the most important information. While accuracy (e.g., experiment start/end point) is sacrificed, the presence of orthogonal spectral components and how they cluster or scatter, may help visualize complex chemical or biological data.

Dynamic spectral datasets were reduced to the first two principal components, PC1 and PC2, (Figure 4C). PC1 corresponds to the highest variance in the dataset, while PC2 corresponds to the next largest variance. The PCA space is a scatter plot containing the variance ratio of each of the variables from the datasets. Clustering between the dissolution experiments (red- and green-colored PC points) suggest the slow spectral variations over time are non-orthogonal to one another. However, for the HDPE melting experiment (red) the PCA space has distinguishable variance. The blue-colored space has the greatest dispersion, indicating crystalline-to-amorphous phase behavior, as reflected by the disappearance of the 729 cm^{-1} band, is uniquely different from that which is observed under dissolution conditions (Figure S9 versus Figure S11). The frequency shifting of the 729 cm^{-1} to lower energy for HDPE melt experiments (Figure 4A and Figure S5) is a consequence of the crystal interactions within the orthorhombic unit cell. As the temperature increases, the crystalline lamellae become disordered; thus, decreasing the overall vibrational interactions within the lattice and reducing the IR frequency. For the dissolution experiments, the shifting of the 729 cm^{-1} band is not observed (first 5 minutes in Figure 4A versus Figure 4B); rather, the $\rho(CH_2)$ mode at 729 cm^{-1} experiences a more immediate decrease in absorbance intensity.

Figure 4 reveals the crystal vibration interactions of PE in film form to have orthogonal spectral components. This suggests thermodynamic and/or kinetic and intermolecular forces should be investigated in future work. Such insights regarding the fundamental phase-behavior for solid-liquid interfacial systems, and the vibrational motions found therein, may be critical for the development of dissolution/precipitation recycling technologies for semi-crystalline polymers.

In addition to the frequency-shifting increase of the amorphous band at 720 cm^{-1} due to *p*-xylene, a tentative origin for the orthogonality of melt versus dissolution de-crystallization behavior at 750-700 cm^{-1} may be attributed to the presence of *gauche* crystal defects such as the tentatively assigned band at 731 cm^{-1} (Section 3.1 and Figure 3). Further characterization of the defects in PE spherulites is needed. Variations in PE chain orientation within lamellar crystals is currently an active research topic [21]. While the PCA analysis supports the orthogonality of spectral components, backing our slow spectral changes observed using 2D-COS, no additional molecular information is provided by PCA at this time. However, future work may explore dimensionality reduction techniques for computational load and/or noise reduction in autonomous high-throughput measurement applications. For example, band selection and assignment techniques in the NIR, as a form of dimensionality reduction, could benefit from the analysis presented here. In addition, coalescence of heterospectral 2D-COS with multi-modality technologies (MIR, NIR, and other spectroscopic probes) may provide a way to maximize scientific feedback for dynamic molecular systems that are otherwise limited in a particular frequency range (e.g., black-pigmented plastic waste

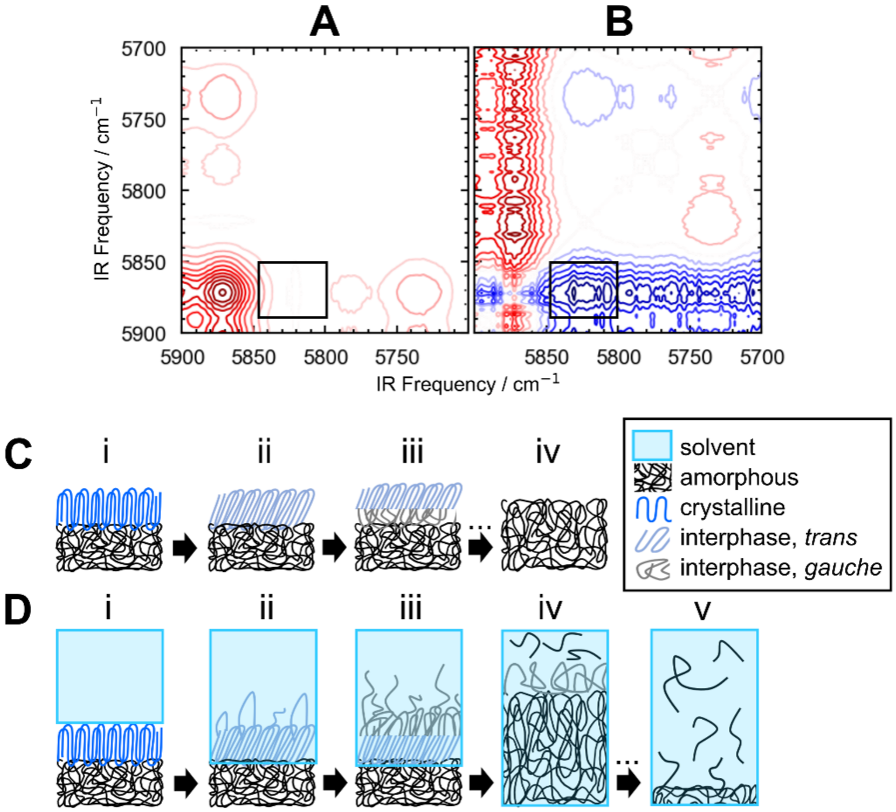

FIGURE 5. LLDPE/*p*-xylene at 106 °C; 31 seconds elapsed. (A) Synchronous spectrum 5900-5700 cm^{-1}. (B) Asynchronous spectrum 5900-5700 cm^{-1}; the black box contains a band corresponding to the terminal CH_3 first overtone at 5830 cm^{-1}. Red color representing positive correlation intensity and blue for negative. Tentative PE decrystallization mechanism. (C) Melting. (C-i) Crystalline and amorphous PE. (C-ii,iii) Heat applied to the system generates the interphase, with the rigid-amorphous layer next to the bulk amorphous layer. (C-iv) After complete decrystallization, the polymer exhibits minimal swelling relative to (D) that represents dissolution; chain branches are omitted for clarity. (D-i) Semi-crystalline PE-solvent interface. (D-ii,iii) Decrystallization occurs along the spherulite-solvent interface where small solvent molecule diffusion induces a force against the chains, resulting in polymer swelling and interphase formation. PE cilia unravel at the crystal/solvent region as the chain conformation changes from *trans* to *gauche*. (D-iv) The rigid amorphous layer first appears at the solid-liquid interface before becoming the highly-mobile amorphous phase. (D-v) Chain diffusion into solvent. *Note:* This mechanism is tentative and focuses on the cilia-relevant modes in (B) that jump in IR frequency when in the presence of solvent; thus, this mechanism is reserved for the hypothetical instance when a *crystalline domain* is directly exposed to a solvent. Indeed, a monolayer PE surface has both crystalline and amorphous domains exposed, as the amorphous layer may surround or envelop the crystalline regions. Future work characterizing PE decrystallization for different chain structures in time and three-dimensional space will help address unanswered questions about temporal events at the molecular level.

is challenging to sort using NIR wavelengths due to the high absorption coefficients).

3.4 Terminal CH_3 Overtones: LDPE Dissolution

2D-COS achieved enhanced spectral resolution in the NIR, a region that may contain new details about polymer decrystallization via the presence of overtone bands corresponding to branch end groups. Figure 5 presents evidence of the terminal CH_3 groups of LLDPE under dissolution at 106 °C. In place of HDPE, LLDPE was chosen due to its lower density, increased branching ratio, and greater population of terminal CH_3 modes. Empirical observations of the CH_3 groups, which correspond to PE cilia, may provide fundamental insights about surface and interphase dynamics of semi-crystalline polymer/liquid systems. Moreover, in the context of chemical recycling, there are two primary research fields: dissolution/precipitation and enzyme hydrolysis. Both procedures depend on the decrystallization, disentanglement, diffusion of polymer chains into solvent, and breakdown of the chains into monomeric units. In particular, the design and deployment of enzymes to convert semi-crystalline polymers into their amorphous phases may benefit from spectroscopic evidence detailing the PE de-crystallization mechanism of PE-containing film materials. Furthermore, and in general, the reduction of energy requirements (e.g., temperature settings and/or impeller stir rate) and increase in dissolution rate is a key development in the polymer recycling field.

Transmission NIR absorbance signals of PE at 5900-5700 cm^{-1} are weak, and they are especially difficult to isolate due to the presence of *p*-xylene which contains a multitude of CH_2 and CH_3 overtones (Figure S13 and S14). While precautions are taken to mitigate the influence of *p*-xylene by performing background subtraction measurements that include the solvent and optical window at the same temperature used for the in-situ experiment, residual solvent overtones remain at 5873 cm^{-1} and 5735 cm^{-1}. However, careful examination of the 5850-5800 cm^{-1} region revealed a tentatively-assigned terminal CH_3 stretch first overtone at 5830 cm^{-1} (Figure 5 and Figure S25).

Unobserved in the synchronous spectrum, Figure 5B shows strong out-of-phase intensities between 5850-5800 cm^{-1}. According to PE spectra literature, the frequency position of the terminal CH_3 first overtone would be expected at 5840-5848 cm^{-1}; however, due to the van der Waals forces governing the solvation structure of the LLDPE chains, the 5845 cm^{-1} band jumps to lower IR frequency. Unlike the gauche amorphous band at 720 cm^{-1} that shifts to higher IR frequency, the 5845 cm^{-1} band shifts to lower IR frequency (Figure S17). Mizushima et al. examined similar NIR absorbance changes of PE melting compared to $C_{14}H_{30}$ and 7-ethyl-$C_{14}H_{29}$ in alkane solvents such as hexane and tetradecane [38]. In Figure 5B, the terminal CH_3 groups appear over 31 seconds, suggesting the PE cilia (i.e., the polymer side/end chains) within the ordered crystalline lamellae first unfold from before changing conformation from *trans* to *gauche*. Unlike the melt environment where the PE chains undergo similar conformational changes during the transition to the disordered amorphous phase, the solvation environment was determined to weaken or loosen the terminal CH_3 overtone vibration. It is likely that the *p*-xylene solvation shell along the LLDPE backbone provides a wider distribution of equilibrium conformation populations (i.e., increased number of solvation structures). Future surface-specific and computational work may explore the solvation layers in polymer/liquid systems to provide greater detail about solvent molecule orientation at the center of and around the terminal CH_3 groups of a given chain.

3.5 Proposed Mechanism: Melting and Dissolution

Figures 5C and 5D present a schematic of the tentative decrystallization mechanism of PE under melting and dissolution conditions, respectively. Based on recent empirical [33,40] and computational [38,44] reports, including the observations reported herein, three remarkable differences are shown in Figures 5C and 5D, namely: (1) swelling of PE thin films under dissolution conditions is significantly greater than that of films under melting conditions which implies that the forces applied to the crystalline lamellae are also greater, (2) orthogonal spectral components corresponding to the $\rho(CH_2)$ modes suggests alterations in the "order-of-events" in which *trans* conformers transition to *gauche* conformers, and (3) terminal CH_3 groups corresponding to unraveling PE cilia become immersed in solution courtesy of a solvation shell provided by *p*-xylene. It is expected that a high crystallinity domain at the surface may show higher solvent resistance than amorphous regions and that edge chains of the crystalline surface domains may be more prone to solvent-induced conformational changes than the middle chains [17]. Future experiments leveraging reflectance spectroscopic measurements (e.g., IR reflection-absorption spectroscopy) or interface-specific non-linear spectroscopic measurements (e.g., vibrational sum-frequency generation spectroscopy) may prove critical in elucidating the dynamic changes at surfaces [108]. For example, X-ray scattering measurements (e.g., small angle X-ray scattering, SAXS) would provide three-dimensional nano-scale structural information of the unperturbed samples, a characterization method that may assist with the interpretation of the anisotropic nature of heterogeneous polymers since injection- and blow-molded PE likely contain variations in macromolecules and crystallite layers.[75] Furthermore, the analysis of conformational changes in-situ may assist with the characterization of temperature- or pressure-generated gradients in thin polymer films.[30]

3.6 Quantification of Degree of Crystallinity: Mid- and Near-Infrared Spectroscopy

Hagemann *et al.* [81] first reported an FT-IR method for the approximating PE crystallinity using a lineshape procedure. Specifically, two MIR spectral regions were assessed: the $\rho(CH_2)$ modes at 750-700 cm^{-1} and the $\delta(CH_2)$ modes at 1500-1400 cm^{-1}. Since then, there have been no reports detailing a quantitative lineshape-fitting procedure for the other semi-crystalline regions. Moreover, there has been a lack of experimental evidence detailing the correlation of MIR and NIR vibrational modes under melting and dissolution conditions. Quantitative insights regarding the mechanical properties of PE are critical if dissolution/precipitation plastics recycling and up-cycling technologies are to be made practical. Furthermore, the development of high-throughput autonomous screening devices that are capable of extracting physical and chemical properties from recyclable materials with unknown composition may hinge on fundamental insights provided by downstream recycling challenges.

Temperature-controlled ATR-FTIR experiments were performed in order to establish a band-fitting procedure for the quantification of PE degree of crystallinity (Equation 1 and Equation 2) in film and pellet samples. The following regions were examined: 750-700 cm^{-1}, 1500-1400 cm^{-1}, 3000-2800 cm^{-1}, and 4400-4200 cm^{-1}. Prior to this study, the melting behavior in the 3000-2800 cm^{-1} spectral region was not reported. Moreover, the transmission FT-IR spectra in the C-H stretching region were found to be absent in previous reports. This is possibly due to the higher absorption coefficient of the vibrational bands in this range. For the 4400-

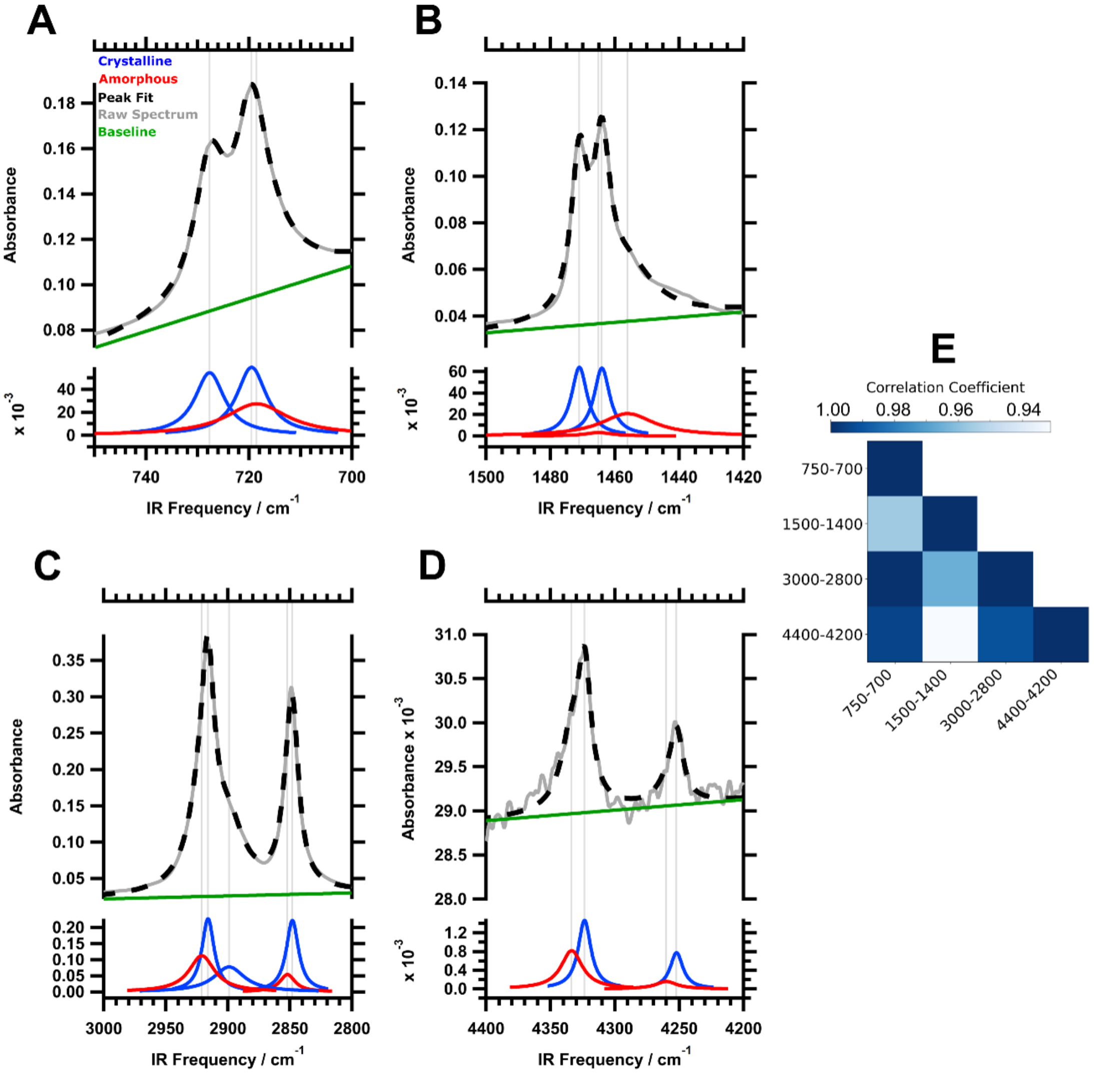

FIGURE 6. IR band-fitting of HDPE semi-crystalline regions at room temperature (A) 750-700 cm^{-1} (B) 1500-1420 cm^{-1} (C) 3000-2800 cm^{-1} (D) 4400-4200 cm^{-1}. Original spectrum (gray); fit spectrum (black dashed); crystalline band (blue); amorphous band (red); linear baseline (green). (E) Half correlation matrix of HDPE degree of crystallinity determined via ATR-FTIR at 22±1 °C until complete de-crystallization.

4200 cm^{-1} region, this is likely due to limited spectrometer setups capable of acquiring dynamic MIR and NIR spectra in a single measurement.

In this study, a surface-sensitive technique, ATR-FTIR spectroscopy, acquired dynamic 1D IR spectra suitable for quantification. It is important to caution that changes observed across the four quantified regions contain vibrational information at different depths in the polymer films. This is due to the evanescent wave generated at the ZnSe/PE interface. The depth of penetration at 816 cm^{-1}, 1460 cm^{-1}, 2900 cm^{-1}, and 4300 cm^{-1} were determined to be 1.47 μm, 0.791 μm, 0.407 μm, and 0.242 μm, respectively (Equation S1). Depending on whether the postconsumer plastic has fillers or surface-migrating slip agents, the vibrational signatures may vary across the semi-crystalline PE bulk or surface regions.[109] The quantification of the semi-crystalline PE regions via ATR-FTIR will benefit the plastics recycling chemistry field because the ν(CH_2) modes have recently been deemed to be key in the development of MIR screening devices.[5] Quantification of these regions using the semi-empirical model reported herein may help with autonomous sorting of HDPE and LDPE consumer plastics [110].

Figures 6A-6D present the band fitting lineshapes for the semi-crystalline PE regions. MIR and NIR bands corresponding to PE's orthorhombic crystalline phase are shown in blue and, at ambient conditions, they represent the majority of the overall lineshape area for each region. The intrinsic band areas of the crystalline and amorphous fractions were approximated using spectra that were acquired at room temperature (22±1 °C) and at pure melt (i.e., complete disordering of polymer chains). Future work may involve the characterization of lineshapes at cryogenic conditions to enhance model parameters.

A key advancement in this work is the utility of 2D-COS to reveal the presence of often-overlooked MIR bands such as 712 cm^{-1}, 731 cm^{-1}, and 1456 cm^{-1} that may be important components in quantitative PE models. In Figure 6A, the bands at 712 cm^{-1} and 713 cm^{-1} were omitted because their influence in the calculations proved trivial. However, for the band at 1456 cm^{-1} corresponding to amorphous short *trans* sequences, this lineshape was factored-in to Equation 1 and Equation 2 for its marked increase in absorbance profile during melting. It may be concluded from these findings that, depending on the sample (i.e., co-monomer, doped sample, lamellar thickness, structural orientation), the presence of all IR-active vibrational modes should be considered during the FT-IR quantification of degree of crystallinity, and only be ruled-out if the contributions to the overall lineshape are deemed trivial (see Supporting Information for further details regarding the lineshape parameters that were evaluated in this study).

To ensure the robustness and reproducibility of the quantitative FT-IR method, DSC experiments were performed on HDPE pellet samples (Figure S2 and Table S1). The starting x_c values obtained from the FT-IR method were scaled to the x_c values obtained from the second DSC cycle to provide a best approximation for absolute crystallinity. Lanyi *et al.* provide helpful insights about relative versus absolute degree of crystallinity determinations of polypropylene fibers and non-wovens, as absolute values strongly depend on the experiment used to calculate enthalpy of fusion, which may vary up to 10 % [109]. Pellets were chosen for their rigidity and ability to be kept in close contact with the ATR crystal. X_c of the HDPE samples was determined to be 64.9 % via DSC. This value agreed with the averaged FT-IR result of 65.2 % from three independent experiments on different samples. While HDPE was chosen as a model polyolefin for its high crystalline component, LDPE and LLDPE were also investigated to provide baseline measurements and quantifications for other researchers (Table S3). The quantitative FT-IR method correctly assigned a higher X_c to the LLDPE samples over LDPE, a result that aligned with the DSC. Future investigations of the melt dynamics of cilia chain unfolding may improve the modeling of polyolefins that have a higher degrees of chain branching and/or greater variations in chain length.

Figure 6E presents the correlation matrix of the decrystallization trends of three different HDPE melt trials based on the corresponding fitted areas. A positive, linear correlation is observed across all four regions, as each of the values was greater than +0.93. This strong correlation is likely attributed to the intrinsic crystal arrangement found in each region. The $\rho(CH_2)$, $\delta(CH_2)$, $\nu(CH_2)$, $\nu(CH_3)$, and $\nu(CH_2) + \delta(CH_2)$ modes may be leveraged in PE systems where one or more IR regions are un-quantifiable either due to poor signal-to-noise, solvent signal interference, or economic considerations for MIR or NIR instrumentation.

4 Conclusion

A temperature-controlled FT-IR setup was designed and assembled for real-time, in-situ, PE film melting and dissolution experiments. Hetero-spectral 2D-COS revealed hidden IR-active modes that may play a key role in elucidating morphological changes occurrent at the PE-liquid interface. Specifically, temporal spectral changes across four semi-crystalline infrared regions in HDPE, LDPE, and LLDPE were treated via a cross-correlation analysis to provide lineshape fitting parameters for in-situ quantifications of degree of crystallinity. From this study's dissolution experiments, PE's highly mobile gauche conformers were found to shift to higher or lower IR frequency by interactions with the *p*-xylene solvation shell. Dissolution of LDPE films provided evidence of the terminal CH_3 groups of dangling cilia that unravel from crystalline lamellae. These observations may be useful for researchers interested in elucidating the structural changes of the so-called interphase between crystalline and amorphous domains. Future work may investigate how alterations in molecular weight, branching ratio, deuteration, and solvent may influence the dissolution of PE. Lastly, the vibrational spectra and structural insights reported herein may be helpful for chemical recycling researchers seeking to circumvent the issue that rigid crystalline domains pose to polymer-assimilating enzymes.

Acknowledgements

The authors acknowledge the U.S. National Science Foundation (NSF-EFRI E3P) award no. EFMA-2029375 "Valorization of Plastic Waste via Advanced Separation and Processing" for providing financial support. We acknowledge partial support from NSF CAREER grant CHE-1753207 (LV). For the support of LJB, the authors acknowledge funding from the Plastic Recycling and Advanced Chemical-physical Transformations for Improved Circular Economy Research Experience for Undergraduates program (PRACTICE-REU, U.S. NSF Award No. EEC-2150424). For the support of CSD, the authors thank Professor Luis Colón (University at Buffalo) and Professor Wilfredo Resto (University of Puerto Rico at Cayey) for funding from the Alfred P. Sloan Foundation (G-2021-17076). The authors thank the EFRI research team at the University at Buffalo for their expertise and helpful discussions: Professors Javid Rzayev, Michael Shelly, Amit Goyal, Thomas Thundat, John D. Atkinson, Karthik Dantu, and Alan Rae. NS thanks Gabrielle Kerr for assistance acquiring the enthalpy of fusion for the PE samples. Lastly, NS thanks Gregory C. Pierce and Stanley S. Stavinski for their chemical insights.

Conflicts of Interest

The authors declare no conflicts of interest.

Supporting Information.

Additional supporting information can be found online in the Supporting Information section.

Thin film preparation; DSC of HDPE/LDPE/LLDPE; FT-IR of HDPE/*p*-xylene/interference fringes; 2D-COS results from spectral processing methods; PCA train/test set ratio quantification; Quantification parameters of PE crystallinity via FT-IR

Abbreviations

2D-COS, Two-dimensional correlation spectroscopy; HDPE, high-density polyethylene; MIR, mid-infrared; NIR, near-infrared; FT-IR, Fourier-Transform IR spectroscopy; PID, Proportional-Integral-Derivative; PCA, principal component analysis; ZnSe, zinc selenide.

References

1. U. S. Chaudhari, Y. Lin, V. S. Thompson, R. M. Handler, J. M. Pearce, G. Caneba, P. Muhuri, D. Watkins, D. R. Shonnard, "Systems Analysis Approach to Polyethylene Terephthalate and Olefin Plastics Supply Chains in the Circular Economy: A Review of Data Sets and Models", *ACS Sustainable Chemistry & Engineering*, *9* (2021): 7403-7421, https://doi.org/10.1021/acssuschemeng.0c08622.
2. Plastics - the Facts 2022; Plastics Europe, **2022**, https://plasticseurope.org/knowledge-hub/plastics-the-facts-2022/.
3. M. Larrain, S. Van Passel, G. Thomassen, B. Van Gorp, T. T. Nhu, S. Huysveld, K. M. Van Geem, S. De Meester, P. Billen, "Techno-economic assessment of mechanical recycling of challenging post-consumer plastic packaging waste", *Resources, Conservation and Recycling*, *170* (2021): 105607, https://doi.org/10.1016/j.resconrec.2021.105607.
4. B. P. Sutliff, S. Goyal, T. B. Martin, P. A. Beaucage, D. J. Audus, S. V. Orski, "Correlating Near-Infrared Spectra to Bulk Properties in Polyolefins", *Macromolecules*, (2024), https://doi.org/10.1021/acs.macromol.3c02290.
5. N. Stavinski, V. Maheshkar, S. Thomas, K. Dantu, L. Velarde, "Mid-infrared spectroscopy and machine learning for postconsumer plastics recycling", *Environmental Science: Advances*, *2* (2023): 1099-1109, https://doi.org/10.1039/D3VA00111C.
6. F. Long, S. Jiang, A. G. Adekunle, V. M Zavala, E. Bar-Ziv, "Online Characterization of Mixed Plastic Waste Using Machine Learning and Mid-Infrared Spectroscopy", *ACS Sustainable Chemistry & Engineering*, *10* (2022): 16064-16069, https://doi.org/10.1021/acssuschemeng.2c06052.
7. S. Zinchik, S. Jiang, S. Friis, F. Long, L. Høgstedt, V. M. Zavala, E. Bar-Ziv, "Accurate Characterization of Mixed Plastic Waste Using Machine Learning and Fast Infrared Spectroscopy", *ACS Sustainable Chemistry & Engineering*, *9* (2021): 14143-14151, https://doi.org/10.1021/acssuschemeng.1c04281.
8. S. Ferchichi, N. Sheibat-Othman, O. Boyron, C. Bonnin, S. Norsic, M. Rey-Bayle, V. Monteil, "In situ dissolved polypropylene prediction by Raman and ATR-IR spectroscopy for its recycling", *Analytical Methods*, *16* (2024): 3109-3117, https://doi.org/10.1039/D4AY00667D.
9. K. L. Sánchez-Rivera, A. d. C. Munguía-López, P. Zhou, V. S. Cecon, J. Yu, K. Nelson, D. Miller, S. Grey, Z. Xu, E. Bar-Ziv, K. L. Vorst, G. W. Curtzwiler, R. C. Van Lehn, V. M. Zavala, G. W. Huber, "Recycling of a post-industrial printed multilayer plastic film containing polyurethane inks by solvent-targeted recovery and precipitation", *Resources, Conservation and Recycling*, *197* (2023): 107086, https://doi.org/10.1016/j.resconrec.2023.107086.
10. A. d. C. Munguía-López, D. Göreke, K. L. Sánchez-Rivera, H. A. Aguirre-Villegas, S. Avraamidou, G. W. Huber, V. M. Zavala, "Quantifying the environmental benefits of a solvent-based separation process for multilayer plastic films", *Green Chemistry*, *25* (2023): 1611-1625, https://doi.org/10.1039/D2GC04262B.
11. U. S. Chaudhari, D. G. Kulas, A. Peralta, T. Hossain, A. T. Johnson, D. S. Hartley, R. M. Handler, B. K. Reck, V. S. Thompson, D. W. Watkins, D. R. Shonnard, "Solvent based dissolution–precipitation of waste polyethylene terephthalate: economic and environmental performance metrics", *RSC Sustainability*, *1* (2023): 1849-1860, https://doi.org/10.1039/D3SU00231D.
12. G. D. Mumbach, R. de Sousa Cunha, R. A. F. Machado, A. Bolzan, "Dissolution of adhesive resins present in plastic waste to recover polyolefin by sink-float separation processes", *Journal of Environmental Management*, *243* (2019): 453-462, https://doi.org/10.1016/j.jenvman.2019.05.021.
13. N. Gama, G. Silva, B. Godinho, A. Ferreira, M. Rodrigues, J. A. P. Coutinho, "Recycling of a Polymer Mixture Through Dissolution–Precipitation and Development of Machine Learning Models to Assess Polymer/Solvent Suitability", *Journal of Polymer Science*, *n/a*, https://doi.org/10.1002/pol.20241131.
14. M. Ghasemi, P. Alexandridis, M. Tsianou, "Dissolution of Cellulosic Fibers: Impact of Crystallinity and Fiber Diameter", *Biomacromolecules*, *19* (2018): 640-651, https://doi.org/10.1021/acs.biomac.7b01745.
15. M. Ghasemi, A. Y. Singapati, M. Tsianou, P. Alexandridis, "Dissolution of semicrystalline polymer fibers: Numerical modeling and parametric analysis", *AIChE Journal*, *63* (2017): 1368-1383, https://doi.org/10.1002/aic.15615.
16. M. Ghasemi, M. Tsianou, P. Alexandridis, "Assessment of solvents for cellulose dissolution", *Bioresource Technology*, *228* (2017): 330-338, https://doi.org/10.1016/j.biortech.2016.12.049.
17. D. Lazarenko, G. P. Schmidt, M. F. Crowley, G. T. Beckham, B. C. Knott, "Molecular Details of Polyester Decrystallization via Molecular Simulation", *Macromolecules*, (2025): ASAP, https://doi.org/10.1021/acs.macromol.4c02130.
18. R. Kol, R. Denolf, G. Bernaert, D. Manhaeghe, E. Bar-Ziv, G. W. Huber, N. Niessner, M. Verswyvel, A. Lemonidou, D. S. Achilias, S. De Meester, "Increasing the Dissolution Rate of Polystyrene Waste in Solvent-Based Recycling", *ACS Sustainable Chemistry & Engineering*, *12* (2024): 4619-4630, https://doi.org/10.1021/acssuschemeng.3c08154.
19. M. Tasumi, S. Krimm, "Crystal Vibrations of Polyethylene", *The Journal of Chemical Physics*, *46* (1967): 755-766, https://doi.org/10.1063/1.1840736.
20. J.-M. Lagaron, "The factor group splitting phenomenon: a vibrational spectroscopy approach to assess polymer crystallinity and crystalline density", *Macromolecular Symposia*, *184* (2002): 19-36, https://doi.org/10.1002/1521-3900(200208)184:1<19::AID-MASY19>3.0.CO;2-X.
21. S. Kanomi, H. Marubayashi, T. Miyata, H. Jinnai, "Reassessing chain tilt in the lamellar crystals of polyethylene", *Nature Communications*, *14* (2023): 5531, https://doi.org/10.1038/s41467-023-41138-4.

22. D. M. Dattelbaum, E. D. Emmons, A. M. Covington, L. L. Stevens, N. Velisavljevic, B. Branch, "High-pressure X-ray diffraction and vibrational spectroscopy of polyethylene: Evidence for a structural phase transition", *Vibrational Spectroscopy*, *111* (2020): 103173, https://doi.org/10.1016/j.vibspec.2020.103173.

23. L. Fontana, D. Q. Vinh, M. Santoro, S. Scandolo, F. A. Gorelli, R. Bini, M. Hanfland, "High-pressure crystalline polyethylene studied by x-ray diffraction and ab initio simulations", *Physical Review B*, *75* (2007): 174112, https://doi.org/10.1103/PhysRevB.75.174112.

24. K. Tashiro, S. Sasaki, M. Kobayashi, "Structural Investigation of Orthorhombic-to-Hexagonal Phase Transition in Polyethylene Crystal: The Experimental Confirmation of the Conformationally Disordered Structure by X-ray Diffraction and Infrared/Raman Spectroscopic Measurements", *Macromolecules*, *29* (1996): 7460-7469, https://doi.org/10.1021/ma960333+.

25. F. M. Mirabella, A. Bafna, "Determination of the crystallinity of polyethylene/α-olefin copolymers by thermal analysis: Relationship of the heat of fusion of 100% polyethylene crystal and the density", *Journal of Polymer Science Part B: Polymer Physics*, *40* (2002): 1637-1643, https://doi.org/10.1002/polb.10228.

26. J. A. H. M. Moonen, W. A. C. Roovers, R. J. Meier, B. J. Kip, "Crystal and molecular deformation in strained high-performance polyethylene fibers studied by wide-angle x-ray scattering and Raman spectroscopy", *Journal of Polymer Science Part B: Polymer Physics*, *30* (1992): 361-372, https://doi.org/10.1002/polb.1992.090300406.

27. S. C. Averett, S. K. Stanley, J. J. Hanson, S. J. Smith, J. E. Patterson, "Surface Spectroscopic Signatures of Mechanical Deformation in High-Density Polyethylene (HDPE)", *Applied Spectroscopy*, *72* (2018): 1057-1068, https://doi.org/10.1177/0003702818757232.

28. T. Tsukame, M. Kutsuzawa, H. Sekine, H. Saitoh, Y. Shibasaki, "Identification of Polyethylene by Differential Scanning Calorimetry: Application to forensic science", *Journal of Thermal Analysis and Calorimetry*, *57* (1999): 847-851, https://doi.org/10.1023/a:1010106612095.

29. E. Földes, G. Keresztury, M. Iring, F. Tüdős, "Crystallinity of polyethylene measured by density, DSC, and raman spectroscopy. A comparison", *Die Angewandte Makromolekulare Chemie*, *187* (1991): 87-99, https://doi.org/10.1002/apmc.1991.051870109.

30. M. Nabata, T. Kida, Y. Hiejima, K.-h. Nitta, "In-situ Raman spectroscopic study of conformational reorganization during heat treatment for high-density polyethylene solid", *Polymer*, *290* (2024): 126558, https://doi.org/10.1016/j.polymer.2023.126558.

31. M. Bredács, C. Barretta, L. F. Castillon, A. Frank, G. Oreski, G. Pinter, S. Gergely, "Prediction of polyethylene density from FTIR and Raman spectroscopy using multivariate data analysis", *Polymer Testing*, *104* (2021): 107406, https://doi.org/10.1016/j.polymertesting.2021.107406.

32. A. Z. Samuel, B.-H. Lai, S.-T. Lan, M. Ando, C.-L. Wang, H.-o. Hamaguchi, "Estimating Percent Crystallinity of Polyethylene as a Function of Temperature by Raman Spectroscopy Multivariate Curve Resolution by Alternating Least Squares", *Analytical Chemistry*, *89* (2017): 3043-3050, https://doi.org/10.1021/acs.analchem.6b04750.

33. Y. Jin, A. P. Kotula, C. R. Snyder, A. R. Hight Walker, K. B. Migler, Y. J. Lee, "Raman Identification of Multiple Melting Peaks of Polyethylene", *Macromolecules*, *50* (2017): 6174-6183, https://doi.org/10.1021/acs.macromol.7b01055.

34. F. Rull, A. C. Prieto, J. M. Casado, F. Sobron, H. G. M. Edwards, "Estimation of crystallinity in polyethylene by Raman spectroscopy", *Journal of Raman Spectroscopy*, *24* (1993): 545-550, https://doi.org/10.1002/jrs.1250240813.

35. G. Strobl, W. Hagedorn, "Raman spectroscopic method for determining the crystallinity of polyethylene", *Journal of Polymer Science: Polymer Physics Edition*, *16* (1978): 1181-1193, https://doi.org/10.1002/pol.1978.180160704.

36. M. R. Jung, F. D. Horgen, S. V. Orski, V. Rodriguez C, K. L. Beers, G. H. Balazs, T. T. Jones, T. M. Work, K. C. Brignac, S.-J. Royer, K. D. Hyrenbach, B. A. Jensen, J. M. Lynch, "Validation of ATR FT-IR to identify polymers of plastic marine debris, including those ingested by marine organisms", *Marine Pollution Bulletin*, *127* (2018): 704-716, https://doi.org/10.1016/j.marpolbul.2017.12.061.

37. L. Zhang, S. Watanabe, I. Noda, Y. Wu, "Spectral inter-conversion analysis of thermally induced structural changes in polyethylene crystals", *Vibrational Spectroscopy*, *60* (2012): 92-97, https://doi.org/10.1016/j.vibspec.2011.10.009.

38. M. Mizushima, T. Kawamura, K. Takahashi, K.-h. Nitta, "In situ near-infrared spectroscopic studies of the structural changes of polyethylene during melting", *Polymer Journal*, *44* (2012): 162-166, https://doi.org/10.1038/pj.2011.100.

39. N. F. Brockmeier, "The effect of temperature on the infrared absorption frequencies of polyethylene and ethylene–propylene copolymer films", *Journal of Applied Polymer Science*, *12* (1968): 2129-2140, https://doi.org/10.1002/app.1968.070120916.

40. A. Tapash, P. J. DesLauriers, J. L. White, "Simple NMR Experiments Reveal the Influence of Chain Length and Chain Architecture on the Crystalline/Amorphous Interface in Polyethylenes", *Macromolecules*, *48* (2015): 3040-3048, https://doi.org/10.1021/acs.macromol.5b00475.

41. M. de Langen, K. O. Prins, "Mobility of polyethylene chains in the orthorhombic and hexagonal phases investigated by NMR", *Chemical Physics Letters*, *299* (1999): 195-200, https://doi.org/10.1016/S0009-2614(98)01250-0.

42. I. A. Strelnikov, E. A. Zubova, "Monoclinic Phase and Competition Between Transformation Modes in the Phase Transition Between Orthorhombic and Triclinic Phases of Crystalline Polyethylene", *Macromolecular Research*, *29* (2021): 851-854, https://doi.org/10.1007/s13233-021-9101-9.

43. I.-C. Yeh, J. L. Lenhart, G. C. Rutledge, J. W. Andzelm, "Molecular Dynamics Simulation of the Effects of Layer Thickness and Chain Tilt on Tensile Deformation Mechanisms of Semicrystalline Polyethylene", *Macromolecules*, *50* (2017): 1700-1712, https://doi.org/10.1021/acs.macromol.6b01748.

44. A. L. Brayton, I.-C. Yeh, J. W. Andzelm, G. C. Rutledge, "Vibrational Analysis of Semicrystalline Polyethylene Using Molecular Dynamics Simulation", *Macromolecules*, *50* (2017): 6690-6701, https://doi.org/10.1021/acs.macromol.7b00995.

45. E. A. Zubova, N. K. Balabaev, L. I. Manevitch, "Molecular mechanisms of the chain diffusion between crystalline and amorphous fractions in polyethylene", *Polymer*, *48* (2007): 1802-1813, https://doi.org/10.1016/j.polymer.2006.12.032.

46. E. Agosti, G. Zerbi, I. M. Ward, "Structure of the skin and core of ultradrawn polyethylene films by vibrational spectroscopy", *Polymer*, *33* (1992): 4219-4229, https://doi.org/10.1016/0032-3861(92)90261-T.

47. I. Noda, "Two-dimensional infrared spectroscopy", *Journal of the American Chemical Society*, *111* (1989): 8116-8118, https://doi.org/10.1021/ja00203a008.

48. I. Noda, "Generalized Two-Dimensional Correlation Method Applicable to Infrared, Raman, and other Types of Spectroscopy",

Applied Spectroscopy, *47* (1993): 1329-1336, https://doi.org/10.1366/0003702934067694.

49. I. Noda, "Two-Dimensional Infrared (2D IR) Spectroscopy: Theory and Applications", *Applied Spectroscopy*, *44* (1990): 550-561, https://doi.org/10.1366/0003702904087398.

50. I. Noda, "Frontiers of Two-Dimensional Correlation Spectroscopy. Part 1. New concepts and noteworthy developments", *Journal of Molecular Structure*, *1069* (2014): 3-22, https://doi.org/10.1016/j.molstruc.2014.01.025.

51. I. Noda, "Two-trace two-dimensional (2T2D) correlation spectroscopy – A method for extracting useful information from a pair of spectra", *Journal of Molecular Structure*, *1160* (2018): 471-478, https://doi.org/10.1016/j.molstruc.2018.01.091.

52. I. Noda, Y. Ozaki. Two-dimensional correlation spectroscopy: applications in vibrational and optical spectroscopy; John Wiley & Sons, **2005**.

53. T. Otosu, K. Ishii, H. Oikawa, M. Arai, S. Takahashi, T. Tahara, "Highly Heterogeneous Nature of the Native and Unfolded States of the B Domain of Protein A Revealed by Two-Dimensional Fluorescence Lifetime Correlation Spectroscopy", *The Journal of Physical Chemistry B*, *121* (2017): 5463-5473, https://doi.org/10.1021/acs.jpcb.7b00546.

54. A. Litwińczuk, S. R. Ryu, L. A. Nafie, J. W. Lee, H. I. Kim, Y. M. Jung, B. Czarnik-Matusewicz, "The transition from the native to the acid-state characterized by multi-spectroscopy approach: Study for the holo-form of bovine α-lactalbumin", *Biochimica et Biophysica Acta (BBA) - Proteins and Proteomics*, *1844* (2014): 593-606, https://doi.org/10.1016/j.bbapap.2013.12.018.

55. L. Ma, Z. Ahmed, S. A. Asher, "Ultraviolet Resonance Raman Study of Side Chain Electrostatic Control of Poly-l-Lysine Conformation", *The Journal of Physical Chemistry B*, *115* (2011): 4251-4258, https://doi.org/10.1021/jp2005343.

56. S. Navea, A. de Juan, R. Tauler, "Modeling Temperature-Dependent Protein Structural Transitions by Combined Near-IR and Mid-IR Spectroscopies and Multivariate Curve Resolution", *Analytical Chemistry*, *75* (2003): 5592-5601, https://doi.org/10.1021/ac0343883.

57. K. Murayama, Y. Wu, B. Czarnik-Matusewicz, Y. Ozaki, "Two-Dimensional/Attenuated Total Reflection Infrared Correlation Spectroscopy Studies on Secondary Structural Changes in Human Serum Albumin in Aqueous Solutions: pH-Dependent Structural Changes in the Secondary Structures and in the Hydrogen Bondings of Side Chains", *The Journal of Physical Chemistry B*, *105* (2001): 4763-4769, https://doi.org/10.1021/jp004537a.

58. D. L. Elmore, R. A. Dluhy, "βν-Correlation Analysis: A Modified Two-Dimensional Infrared Correlation Method for Determining Relative Rates of Intensity Change", *The Journal of Physical Chemistry B*, *105* (2001): 11377-11386, https://doi.org/10.1021/jp0114485.

59. Y.-n. Bao, Y.-w. Zeng, R. Guo, M. Ablikim, H.-f. Shi, L.-m. Yang, Z.-l. Yang, Y.-z. Xu, I. Noda, J.-g. Wu, "Two-dimensional correlation spectroscopic studies on coordination between organic ligands and Ni2+ ions", *Spectrochimica Acta Part A: Molecular and Biomolecular Spectroscopy*, *197* (2018): 126-132, https://doi.org/10.1016/j.saa.2017.12.030.

60. J. Liu, Y. Gao, L. Zheng, D. Gao, A. He, Y. Liu, S. Weng, Y. Zhao, Z. Yang, L. Yang, X. Wen, Y. Xu, I. Noda, J. Wu, "Coordination between cobalt (II) ion and carbonyl group in acetone probed by using DAOSD approach", *Journal of Molecular Structure*, *1069* (2014): 217-222, https://doi.org/10.1016/j.molstruc.2014.02.036.

61. J. Qiu, T. H. Nguyen, S. Kim, Y. J. Lee, M.-T. Song, W.-J. Huang, X.-B. Chen, T. M. H. Nguyen, I.-S. Yang, "Two-dimensional correlation spectroscopy analysis of Raman spectra of NiO nanoparticles", *Spectrochimica Acta Part A: Molecular and Biomolecular Spectroscopy*, *280* (2022): 121498, https://doi.org/10.1016/j.saa.2022.121498.

62. A. Wesełucha-Birczyńska, A. Kołodziej, M. Świętek, P. Moskal, Ł. Skalniak, E. Długoń, M. Błażewicz, "Does 2D correlation Raman spectroscopy distinguish polymer nanomaterials due to the nanoaddition?", *Journal of Molecular Structure*, *1217* (2020): 128342, https://doi.org/10.1016/j.molstruc.2020.128342.

63. A. Kołodziej, A. Wesełucha-Birczyńska, M. Świętek, D. Horák, M. Błażewicz, "A 2D-Raman correlation spectroscopy analysis of the polymeric nanocomposites with magnetic nanoparticles", *Journal of Molecular Structure*, *1215* (2020): 128294, https://doi.org/10.1016/j.molstruc.2020.128294.

64. W. Chen, C. Qian, X.-Y. Liu, H.-Q. Yu, "Two-Dimensional Correlation Spectroscopic Analysis on the Interaction between Humic Acids and TiO2 Nanoparticles", *Environmental Science & Technology*, *48* (2014): 11119-11126, https://doi.org/10.1021/es502502n.

65. P. Lasch, I. Noda, "Two-Dimensional Correlation Spectroscopy for Multimodal Analysis of FT-IR, Raman, and MALDI-TOF MS Hyperspectral Images with Hamster Brain Tissue", *Analytical Chemistry*, *89* (2017): 5008-5016, https://doi.org/10.1021/acs.analchem.7b00332.

66. H. Shinzawa, K. Awa, T. Okumura, S.-i. Morita, M. Otsuka, Y. Ozaki, H. Sato, "Raman imaging analysis of pharmaceutical tablets by two-dimensional (2D) correlation spectroscopy", *Vibrational Spectroscopy*, *51* (2009): 125-131, https://doi.org/10.1016/j.vibspec.2008.11.011.

67. S. Šašić, D. A. Clark, J. C. Mitchell, M. J. Snowden, "Analyzing Raman Maps of Pharmaceutical Products by Sample—Sample Two-Dimensional Correlation", *Applied Spectroscopy*, *59* (2005): 630-638, https://doi.org/10.1366/0003702053946047.

68. L. Gozdzialski, B. Wallace, I. Noda, D. Hore, "Exploring the use of infrared absorption spectroscopy and two-trace two-dimensional correlation analysis for the resolution of multi-component drug mixtures", *Spectrochimica Acta Part A: Molecular and Biomolecular Spectroscopy*, *282* (2022): 121684, https://doi.org/10.1016/j.saa.2022.121684.

69. S. Watanabe, I. Noda, Y. Ozaki, "Thermally induced conformational and structural disordering in polyethylene crystal studied by near-infrared spectroscopy", *Polymer*, *49* (2008): 774-784, https://doi.org/10.1016/j.polymer.2007.12.021.

70. S. Watanabe, I. Noda, Y. Hu, Y. Ozaki, "Thermally induced conformational disordering process in high-density polyethylene crystal studied by generalized two-dimensional correlation mid-infrared spectroscopy", *Polymer*, *48* (2007): 6632-6638, https://doi.org/10.1016/j.polymer.2007.09.001.

71. S. Morita, H. Shinzawa, I. Noda, Y. Ozaki, "Perturbation-Correlation Moving-Window Two-Dimensional Correlation Spectroscopy", *Applied Spectroscopy*, *60* (2006): 398-406, https://opg.optica.org/as/abstract.cfm?URI=as-60-4-398.

72. H. Huang, S. Malkov, M. Coleman, P. Painter, "Application of Two-Dimensional Correlation Infrared Spectroscopy to the Study of Immiscible Polymer Blends", *Macromolecules*, *36* (2003): 8148-8155, https://doi.org/10.1021/ma025945a.

73. B. Liu, W. Li, Y. Xu, H. Zhang, R. Cai, Z. Guo, L. Zhou, J. Zhang, Y. Yuan, "Mechanism of cellulose regeneration from its ionic liquid solution as revealed by infrared spectroscopy",

Polymer, *257* (2022): 125280, https://doi.org/10.1016/j.polymer.2022.125280.
74. T. P. Lodge, "Celebrating 50 Years of Macromolecules", *Macromolecules*, *50* (2017): 9525-9527, https://doi.org/10.1021/acs.macromol.7b02507.
75. E. R.-v. Dorp, B. Möginger, B. Hausnerova, "Thermal expansion of semi-crystalline polymers: Anisotropic thermal strain and crystallite orientation", *Polymer*, *191* (2020): 122249, https://doi.org/10.1016/j.polymer.2020.122249.
76. B. K. Wunderlich, G. Czornyj, "A Study of Equilibrium Melting of Polyethylene", *Macromolecules*, *10* (1977): 906-913, https://doi.org/10.1021/ma60059a006.
77. D. Barron. Buchdahl's Chromatic Co-ordinate Concept Applied To IR Materials; SPIE, **1987**.
78. S. Krimm, C. Y. Liang, G. B. B. M. Sutherland, "Infrared Spectra of High Polymers. II. Polyethylene", *The Journal of Chemical Physics*, *25* (1956): 549-562, https://doi.org/10.1063/1.1742963.
79. P. Tiemblo, J. Guzmán, R. Serrano, M. Hoyos, N. García, "Evidence of a monoclinic-like amorphous phase in composites of LDPE with spherical, fibrous and laminar nanofillers as studied by infrared spectroscopy", *European Polymer Journal*, *45* (2009): 30-39, https://doi.org/10.1016/j.eurpolymj.2008.09.040.
80. P. C. Painter, J. Havens, W. W. Hart, J. L. Koenig, "A fourier transform infrared spectroscopic investigation of polyethylene single crystals. II. Fine structure of the CH2 rocking mode", *Journal of Polymer Science: Polymer Physics Edition*, *15* (1977): 1237-1249, https://doi.org/10.1002/pol.1977.180150709.
81. H. Hagemann, R. G. Snyder, A. J. Peacock, L. Mandelkern, "Quantitative infrared methods for the measurement of crystallinity and its temperature dependence: polyethylene", *Macromolecules*, *22* (1989): 3600-3606, https://doi.org/10.1021/ma00199a017.
82. L. Glatt, J. W. Ellis, "Near Infrared Pleochroism. II. The 0.8–2.5µ Region of Some Linear Polymers", *The Journal of Chemical Physics*, *19* (1951): 449-457, https://doi.org/10.1063/1.1748246.
83. H. Hagemann, H. L. Strauss, R. G. Snyder, "Structure and crystallization of n-C21H44, n-C36H74, and low-molecular-weight polyethylene glasses", *Macromolecules*, *20* (1987): 2810-2819, https://doi.org/10.1021/ma00177a029.
84. S. Watanabe, J. Dybal, K. Tashiro, Y. Ozaki, "A near-infrared study of thermally induced structural changes in polyethylene crystal", *Polymer*, *47* (2006): 2010-2017, https://doi.org/10.1016/j.polymer.2006.01.067.
85. H. Sato, M. Shimoyama, T. Kamiya, T. Amari, S. Šašiç, T. Ninomiya, H. W. Siesler, Y. Ozaki, "Near Infrared Spectra of Pellets and Thin Films of High-Density, Low-Density and Linear Low-Density Polyethylenes and Prediction of Their Physical Properties by Multivariate Data Analysis", *Journal of Near Infrared Spectroscopy*, *11* (2003): 309-321, https://doi.org/10.1255/jnirs.376.
86. N. Fuse, Y. Matsue, S. Morita, "Prediction of breakage in human hair caused by cyclical extension using infrared spectroscopy coupled with multivariate curve resolution", *Analytical Sciences*, *39* (2023): 229-234, https://doi.org/10.1007/s44211-022-00226-z.
87. M. A. Czarnecki, S. Morita, In Near-Infrared Spectroscopy: Theory, Spectral Analysis, Instrumentation, and Applications; Ozaki, Y., Huck, C., Tsuchikawa, S., Engelsen, S. B., Eds.; Springer Singapore: Singapore, **2021**, pp 111-126.
88. S. Morita, "Chemometrics and Related Fields in Python", *Analytical Sciences*, *36* (2020): 107-112, https://doi.org/10.2116/analsci.19R006.
89. H. Yamasaki, S. Morita, "Multivariate curve resolution using a combination of mid-infrared and near-infrared spectra for the analysis of isothermal epoxy curing reaction", *Spectrochimica Acta Part A: Molecular and Biomolecular Spectroscopy*, *197* (2018): 114-120, https://doi.org/10.1016/j.saa.2017.11.043.
90. P. J. Flory, D. Y. Yoon, K. A. Dill, "The interphase in lamellar semicrystalline polymers", *Macromolecules*, *17* (1984): 862-868, https://doi.org/10.1021/ma00134a055.
91. I. Karacan, "Molecular structure and orientation of gel-spun polyethylene fibers", *Journal of Applied Polymer Science*, *101* (2006): 1317-1333, https://doi.org/10.1002/app.22952.
92. A. J. Pennings, A. Zwijnenburg, "Longitudinal growth of polymer crystals from flowing solutions. VI. Melting behavior of continuous fibrillar polyethylene crystals", *Journal of Polymer Science: Polymer Physics Edition*, *17* (1979): 1011-1032, https://doi.org/10.1002/pol.1979.180170610.
93. D. C. Bassett, S. Block, G. J. Piermarini, "A high-pressure phase of polyethylene and chain-extended growth", *Journal of Applied Physics*, *45* (1974): 4146-4150, https://doi.org/10.1063/1.1663028.
94. T. Seto, T. Hara, K. Tanaka, "Phase Transformation and Deformation Processes in Oriented Polyethylene", *Japanese Journal of Applied Physics*, *7* (1968): 31, https://doi.org/10.1143/JJAP.7.31.
95. M. Abdmouleh, I. Jedidi, M. Khitouni, A. Ben Salah, A. Kabadou, "LDPE phase composition in LDPE/Cu composites using thermal analysis and FTIR spectroscopy", *Journal of Applied Spectroscopy*, *78* (2011): 174-182, https://doi.org/10.1007/s10812-011-9443-8.
96. H. Kiho, A. Peterlin, P. H. Geil, "Polymer deformation. VIII. Stability of the monoclinic phase of polyethylene", *Journal of Polymer Science Part B: Polymer Letters*, *3* (1965): 157-160, https://doi.org/10.1002/pol.1965.110030217.
97. E. R. Walter, F. P. Reding, "The appearance of a new crystalline phase in stretched, linear polyethylene", *Journal of Polymer Science*, *21* (1956): 557-559, https://doi.org/10.1002/pol.1956.120219923.
98. P. Bernazzani, V. T. Bich, H. Phuong-Nguyen, A. Haine, C. Chapados, L. H. Dao, G. Delmas, "FTIR analysis of the phase content in low-density polyethylene", *Canadian Journal of Chemistry*, *76* (1998): 1674-1687, https://doi.org/10.1139/v98-159.
99. I. Noda, In Frontiers and Advances in Molecular Spectroscopy; Laane, J., Ed.; Elsevier, **2018**, pp 47-75.
100. T. Abe, H. Shimada, T. Hoshino, D. Kawaguchi, K. Tanaka, "Sum frequency generation imaging for semi-crystalline polymers", *Polymer Journal*, *54* (2022): 679-685, https://doi.org/10.1038/s41428-021-00613-9.
101. Y. He, Y. Zhang, H. Ren, J. Wang, W. Guo, S.-G. Sun, Z. Wang, "Abnormal spectral bands in broadband sum frequency generation induced by bulk absorption and refraction", *Opt. Express*, *27* (2019): 28564-28574, https://doi.org/10.1364/OE.27.028564.
102. D. Zhang, Y. R. Shen, G. A. Somorjai, "Studies of surface structures and compositions of polyethylene and polypropylene by IR+visible sum frequency vibrational spectroscopy", *Chemical Physics Letters*, *281* (1997): 394-400, https://doi.org/10.1016/S0009-2614(97)01311-0.
103. A. B. Mrad, N. Sheibat-Othman, A. P. A. Amorim, R. L. do Rosario, T. F. L. McKenna, "Polyethylene Slurries: Swelling and Solubility", *Macromolecular Reaction Engineering*, *17* (2023): 2300020, https://doi.org/10.1002/mren.202300020.

104. M. D. Porter, T. B. Bright, D. L. Allara, C. E. D. Chidsey, "Spontaneously organized molecular assemblies. 4. Structural characterization of n-alkyl thiol monolayers on gold by optical ellipsometry, infrared spectroscopy, and electrochemistry", *Journal of the American Chemical Society*, *109* (1987): 3559-3568, https://doi.org/10.1021/ja00246a011.
105. R. A. MacPhail, H. L. Strauss, R. G. Snyder, C. A. Elliger, "Carbon-hydrogen stretching modes and the structure of n-alkyl chains. 2. Long, all-trans chains", *The Journal of Physical Chemistry*, *88* (1984): 334-341, https://doi.org/10.1021/j150647a002.
106. R. G. Snyder, H. L. Strauss, C. A. Elliger, "Carbon-hydrogen stretching modes and the structure of n-alkyl chains. 1. Long, disordered chains", *The Journal of Physical Chemistry*, *86* (1982): 5145-5150, https://doi.org/10.1021/j100223a018.
107. S. K. Das, S. Sengupta, L. Velarde, "Interfacial Surfactant Ordering in Thin Films of SDS-Encapsulated Single-Walled Carbon Nanotubes", *The Journal of Physical Chemistry Letters*, *7* (2016): 320-326, https://doi.org/10.1021/acs.jpclett.5b02633.
108. S. T. Algoul, S. Sengupta, T. T. Bui, L. Velarde, "Tuning the Surface Ordering of Self-Assembled Ionic Surfactants on Semiconducting Single-Walled Carbon Nanotubes: Concentration, Tube Diameter, and Counterions", *Langmuir*, *34* (2018): 9279-9288, https://doi.org/10.1021/acs.langmuir.8b01813.
109. F. J. Lanyi, N. Wenzke, J. Kaschta, D. W. Schubert, "A method to reveal bulk and surface crystallinity of Polypropylene by FTIR spectroscopy - Suitable for fibers and nonwovens", *Polymer Testing*, *71* (2018): 49-55, https://doi.org/10.1016/j.polymertesting.2018.08.018.
110. N. Andraju, G. W. Curtzwiler, Y. Ji, E. Kozliak, P. Ranganathan, "Machine-Learning-Based Predictions of Polymer and Postconsumer Recycled Polymer Properties: A Comprehensive Review", *ACS Applied Materials & Interfaces*, *14* (2022): 42771-42790, https://doi.org/10.1021/acsami.2c08301.